

Comprehensive numerical relativity – effective-one-body comparison to inform improvements in waveform models for binary neutron star systems

Tim Dietrich and Tanja Hinderer

Max Planck Institute for Gravitational Physics (Albert Einstein Institute), Am Mühlenberg 1, Potsdam 14476, Germany

(Dated: February 8, 2017)

We present a detailed comparison between tidal effective-one-body (EOB) models and new state-of-the-art numerical relativity simulations for non-spinning binary neutron star systems. This comparison is the most extensive one to date, covering a wide range in the parameter space and encompassing the energetics of the binary, the periastron advance, the time and frequency evolution of the gravitational wave phase for the dominant mode, and several subdominant modes. We consider different EOB models with tidal effects that have been proposed, including the model with dynamical tides of [Phys.Rev.Lett. 116 (2016) no.18, 181101] and the gravitational self-force (GSF) inspired tidal EOB model of [Phys.Rev.Lett. 114 (2015) no.16, 161103]. The EOB model with dynamical tides leads to the best representation of the systems considered here, however, the differences to the GSF-inspired model are small. A common feature is that for systems where matter effects are large, i.e. stiff equations of state or small total masses, all EOB models underestimate the tidal effects and differences to the results from numerical relativity simulations become noticeable near the merger. We analyze this regime to diagnose the shortcomings of the models in the late inspiral, where the two neutron stars are no longer isolated bodies moving in vacuum. Our work will serve to guide further advances in modeling these systems.

I. INTRODUCTION

The recent first detection of gravitational waves (GWs) of merging binary black holes (BBHs) [1, 2] has initiated a new observational era in astronomy. Within the next few years GW detections of neutron star (NS) binaries are also anticipated [3, 4]. These observations will have a unique potential to probe the equation of state (EOS) of the ultradense matter in NS interiors [5–14], which remains one of the major unsolved problems in modern astrophysics.

To successfully extract the EOS information from the GW data requires highly accurate waveform models (templates) in order to perform matched-filtered searches, where the data are cross-correlated with a template bank covering all physical values of the parameters. Constructing sufficiently accurate models requires a detailed understanding of late stages of the binary NS (BNS) coalescence, where matter effects on the GW signal become most prominent. In this regime, one must solve Einstein’s equations together with the equations of general relativistic hydrodynamics, a challenging task that can only be accomplished through numerical relativity (NR) simulations. Over the last few years the physical realism of the NR simulations of BNSs has been significantly advanced by including a refined treatment of magnetic fields and microphysical processes, see e.g. [15–25], and by improving the numerical accuracy of the predicted GW signals [26–32].

Unfortunately, NR simulations are too expensive to create template banks for BNS GW signals. Furthermore, analytical descriptions such as the Post-Newtonian (PN) approach become inaccurate close to the merger and are therefore inadequate for analyzing the regime where tidal effects are largest [9, 33, 34]. A successful way to recast PN results and combine them with in-

formation from NR simulations is the effective-one-body (EOB) formalism [35, 36]. This framework has been refined to devise an accurate, semi-analytical description of the dynamics and GW signals of coalescing BHs with arbitrary spins and mass ratios [37–39]. Tidal effects have also been included in the EOB model, starting with the first analysis [40] that used Newtonian and partial 1PN tidal information [41] and was compared against NR simulations in [42]. Further theoretical developments including 2PN tidal effects in the conservative dynamics [43] and 1PN tidal corrections to the waveform amplitudes [6] have led to an improved tidal EOB model that was tested against results from improved NR simulations with robust error estimates in [29, 44]. More recent work has focused on further advancing the EOB description of tidal effects in different ways. The work of Ref. [45] suggested an EOB model based on the Schwarzschild tidal field together with gravitational self-force (GSF) corrections. The pure GSF-based model underestimates matter effects in the late inspiral, but was augmented by an additional term to develop a model that remains close to NR predictions [31, 46]. Another line of recent work has focused on the enhancement of tidal effects due to the NS’s finite fundamental ($f-$) mode frequency that also leads to an improved performance of the model in comparisons with NR results [47, 48].

To date, EOB – NR comparisons for BNSs have been limited to equal mass systems. Although nearly equal mass systems seem to be common [49, 50], recent observations have also discovered systems with mass ratios of $q = M^A/M^B \sim 1.3$ [51, 52]. The range of pulsar masses that have been accurately determined ($1.17 - 2.01M_\odot$) and ‘in situ’ models, see e.g. [53, 54], also suggest a larger range of the mass ratio. Therefore, in this paper20170207, we go beyond previous work in covering the BNS parameter space by considering mass ratios in

arXiv:1702.02053v1 [gr-qc] 7 Feb 2017

the range $q = 1.0 - 1.5$. Since for unequal-mass systems spherical harmonic modes in the GWs besides the dominant $(\ell, m) = (2, 2)$ mode are larger than for equal masses, we also compare the EOB predictions for the $(2, 1)$, $(3, 3)$, and $(4, 4)$ modes with NR simulations. In addition, we perform a comprehensive study of other important diagnostic quantities to test the performance of the EOB models and gain additional insights. Specifically, we investigate the phase evolution of the $(2, 2)$ mode as a function of the GW frequency, analyze the periastron advance (PA), and study the dynamics of the binary by tracing the binding energy vs. specific orbital angular momentum curve over the inspiral.

In general, as also found in previous EOB-NR comparisons, for most scenarios tidal effects in NR simulations are larger than those predicted by EOB models. The origin of this trend is twofold. On the one hand, tidal EOB models generally underestimate tidal effects present in the last stages of the BNS coalescence because they lack higher PN order tidal terms and physical effects that become relevant once the NSs come into contact shortly before the merger. On the other hand NR simulations tend to overestimate tidal effects since numerical dissipation accelerates the inspiral similar to matter effects. This shows that a reliable error estimate is crucial for a proper numerical relativity- analytical relativity comparison of BNSs.

The paper20170207 is organized as follows. In Sec. II we briefly review the tidal EOB models used in this article. Sec. III describes the configurations we investigate (see in particular Tab. I) and briefly summarizes the NR methods employed in the simulations. We then discuss quantities characterizing the dynamics by considering binding energy vs. angular momentum curves in Sec. IV and the PA in Sec. V. In Sec. VI we compare the EOB and NR waveforms. Finally, we discuss current problems of the EOB models during the last stages of the inspiral for two particular cases and outline aspects requiring further improvements to the EOB model in Sec. VII, where we also show results from combining the models of [46] and [47] as a possibility to further enhance tidal effects in the late inspiral regime. We conclude in Sec. VIII.

Throughout this article, we use geometrical units $c = G = M_\odot = 1$ unless otherwise stated.

II. TIDAL EFFECTIVE-ONE-BODY MODELS

The EOB model [35, 36] meshes results from the PN approximation, valid for any mass ratio but limited to weak gravitational fields, with knowledge of strong-field effects from the test-particle limit. The analytical results are further improved by calibrating parameterized higher-order PN terms in the model to NR data to obtain an accurate description of GW signals from BBH systems [37–39]. The conservative EOB dynamics are

described by the Hamiltonian

$$H_{\text{EOB}} = M\sqrt{1 + 2\nu(H_{\text{eff}} - 1)} - M, \quad (1)$$

with $M = M^A + M^B$ being the total mass and $\nu = M^A M^B / M^2$ the symmetric mass ratio. We use A and B to label the two bodies. The effective Hamiltonian H_{eff} describes a particle of mass $\mu \equiv \nu M$ moving in an effective spacetime. For nonspinning binaries the motion is in a plane and the effective Hamiltonian is given by

$$H_{\text{eff}}^2 = p_{r^*}^2 + A \left(1 + \frac{p_\phi^2}{r^2} + 2(4 - 3\nu) \frac{p_{r^*}^4}{\nu r^2} \right), \quad (2)$$

where p_ϕ is the canonical azimuthal angular momentum per unit reduced mass, $p_{r^*} = p_r / \sqrt{D}$ is a rescaled radial momentum, and A and D are potentials describing the effective spacetime. The EOB potentials considered in this paper20170207 have the form $A = A_{\text{pp}} + A_{\text{tidal}}$ and $D = D_{\text{pp}}$, where "pp" denotes the point-mass part that is used for BBH evolutions (EOB_{BBH}). For A_{pp} we use the result given in Eqs. (A1)-(A2h) of Ref. [48] with the calibration parameter $K = 1.712 - 1.804\nu - 39.77\nu^2 + 103.166\nu^3$ determined in [37]. The potential D is taken from Eq. (A4) of Ref. [48]. These choices correspond to the model SEOBNRv2¹.

We evolve the EOB dynamics using the equations of motion

$$\begin{aligned} \frac{dr}{dt} &= \frac{A}{\sqrt{D}} \frac{\partial H_{\text{EOB}}}{\partial p_{r^*}}, \\ \frac{dp_{r^*}}{dt} &= -\frac{A}{\sqrt{D}} \frac{\partial H_{\text{EOB}}}{\partial r} + \mathcal{F}_r, \end{aligned} \quad (3a)$$

$$\frac{d\phi}{dt} = \frac{\partial H_{\text{EOB}}}{\partial p_\phi}, \quad \frac{dp_\phi}{dt} = \mathcal{F}_\phi. \quad (3b)$$

The factor A/\sqrt{D} arises from the fact that p_{r^*} and r are not canonically conjugate variables. The gravitational radiation reaction forces \mathcal{F}_ϕ and \mathcal{F}_r are constructed from the energy flux through

$$\mathcal{F}_\phi = -\frac{1}{\Omega_\phi} \dot{\mathcal{E}}_{\text{rad}}, \quad \mathcal{F}_r = \frac{p_{r^*}}{p_\phi} \mathcal{F}_\phi, \quad (4)$$

where the energy flux is computed from

$$\dot{\mathcal{E}}_{\text{rad}} = \frac{\Omega_\phi^2}{8\pi} \sum_{\ell=2}^8 \sum_{m=0}^{\ell} m^2 |h_{\ell m}^{\text{F}}|^2. \quad (5)$$

¹ Note that A_{pp} used for the EOB_{adGSF+} model introduced in Sec. II C is slightly different than described above since the public available code of [57] is used, see also [46, 58–60]. The effect of the underlying point particle model on the results will be described in more detail in Appendix C.

TABLE I: Configurations. The first column defines the name of the configuration. The subsequent 9 columns describe the corresponding physical properties: EOS, gravitational mass of the individual stars $M^{A,B}$, baryonic mass of the individual stars $M_b^{A,B}$, stars' compactnesses $\mathcal{C}^{A,B}$, the total dimensionless quadrupolar tidal coupling constant κ_2^T , the initial dimensionless GW frequency $M\omega_{22}^0$, the ADM mass M_{ADM} and angular momentum J_{ADM} from the initial data. The last two columns describe the resolutions employed and whether the outermost refinement level consists of Cartesian boxes or spherical shells, cf. [55, 56].

Name	EOS	M^A	\mathcal{C}^A	M^B	\mathcal{C}^B	κ_2^T	$M\omega_{22}^0$	M_{ADM}	J_{ADM}	Resolutions	Grid Config.
MS1b-138138	MS1b	1.375008	0.1445	1.375008	0.1445	262	0.035	2.728593	8.15792	(R1,R2,R3)	shell
SLy-138138	SLy	1.375004	0.1771	1.375004	0.1771	65	0.036	2.727632	8.00631	(R1,R2,R3)	shell
MS1b-153122	MS1b	1.527797	0.1591	1.222228	0.1299	267	0.035	2.728700	8.03219	(R1,R2,R3)	shell
SLy-153122	SLy	1.527388	0.1976	1.222225	0.1573	69	0.036	2.728071	7.93386	(R1,R2,R3)	box
MS1b-165110	MS1b	1.650025	0.1708	1.100000	0.1182	282	0.035	2.729230	7.79917	(R1,R2,R3)	shell
SLy-165110	SLy	1.650019	0.2149	1.097885	0.1416	78	0.036	2.726620	7.70012	(R1,R2,R3)	box
MS1b-150100	MS1b	1.500016	0.1565	1.000001	0.1085	460	0.030	2.482511	6.65711	(R1,R2,R3)	shell
MS1b-150100-ecc	MS1b	1.500016	0.1565	1.000001	0.1085	460	0.030	2.482230	6.61058	(R1)	box
SLy-150100	SLy	1.500009	0.1938	1.000007	0.1293	138	0.031	2.482086	6.58692	(R1,R2,R3)	box

The sum here is only over positive m since $|h_{\ell-m}^{\text{F}}| = |h_{\ell m}^{\text{F}}|$. The factorized EOB waveforms for point masses are computed from

$$h_{\ell m \text{pp}}^{\text{F}} = h_{\ell m}^{\text{N}} S_{\ell m} T_{\ell m} \rho_{\ell m}^{\ell} N_{\ell m}. \quad (6)$$

The various factors in Eq. (10), are described in detail in [61] and given explicitly in Eqs. (16), (17), and (A1)-(A14h) therein.

A. Adiabatic tides with 2PN Taylor expanded potential: EOB_{adPN}

Adiabatic tidal effects arise when the distorted NS remains in hydrostatic equilibrium. In this case the ratio of its induced multipolar deformation to the perturbing tidal field is a constant related to its Love number k_{ℓ} . The deformation of the NSs changes the energy of the system, which can be captured in the EOB approach by including tidal contributions to the EOB potentials of the form

$$\begin{aligned} A^{\text{tidal}} = & -\alpha_2^{(A)} \hat{A}^{(A)} - \alpha_3^{(A)} \left[1 + \left(\frac{15}{2} X_A - 2 \right) u \right. \\ & \left. + \left(\frac{110}{3} X_A^2 - \frac{311}{24} X_A + \frac{8}{3} \right) u^2 \right] \\ & -\alpha_4^{(A)} + (A \leftrightarrow B). \end{aligned} \quad (7)$$

Here $\alpha_2^{(A)}$ is the Newtonian tidal potential given by

$$\alpha_{\ell}^{(A)} = \frac{2X_B}{X_A} k_{\ell}^{(A)} R_A^{2\ell+1} u^{2\ell+2} \quad (8)$$

where $X_{A,B} = M^{A,B}/M$, R_A is the radius, and $u = 1/r$. The 2PN corrections to the tidal potential $\hat{A}^{(A)}$ from Eqs. (6.6) and (6.18) of Ref. [43] are given by

$$\hat{A}_{\text{adPN}}^{(A)} = 1 + \frac{5}{2} X_A u + \left(\frac{337}{28} X_A^2 + \frac{1}{8} X_A + 3 \right) u^2 \quad (9)$$

Tidal effects also influence the dissipative sector since the tidal bulges contribute to the gravitational radiation. In the EOB model this is accounted for by adding to the waveform modes of Eq. (6) a tidal contribution $h_{\ell m}^{\text{tidal}}$ to the GW modes so that

$$h_{\ell m}^{\text{F}} = h_{\ell m \text{pp}}^{\text{F}} + h_{\ell m}^{\text{tidal}}. \quad (10)$$

The explicit results for the adiabatic tidal terms $h_{\ell m}^{\text{tidal}}$ were worked out in Eqs. (A14)-(A17) of Ref. [6] for $l \leq 3$. We use only those terms from Ref. [6] for which the PN knowledge of tidal effects is complete.

B. Dynamical tides with 2PN Taylor expanded potential: EOB_{dyPN}

Dynamical tides become important when the tidal forcing frequency due to the companion's orbital motion approaches an eigenfrequency of the NS's normal modes of oscillation. The inclusion of the effects of dynamic tides from the NS's f -modes of oscillation is discussed in detail in Ref. [48]. Here, we consider only the most practical yet approximate of the models devised therein, where the potential from Eqs. (7) and (9) is used but with k_{ℓ} multiplied by a frequency-dependent enhancement factor such that $k_{\ell} \rightarrow k_{\ell} \hat{k}_{\ell \text{dyn}}$ with

$$\begin{aligned} \hat{k}_{\ell \text{dyn}} = & a_{\ell} + b_{\ell} \left[\frac{\omega_{0\ell}^2}{\omega_{0\ell}^2 - (m\Omega)^2} + \frac{\omega_{0\ell}^2}{2\sqrt{\epsilon_m} \hat{t}\Omega' (m\Omega)^2} \right. \\ & \left. + \frac{\sqrt{\pi} \omega_{0\ell}^2}{\sqrt{3} \sqrt{\epsilon_m} (m\Omega)^2} \mathcal{Q}_{\ell m} \right]. \end{aligned} \quad (11)$$

Here, $\Omega' = 3/8$, $\Omega = M^{1/2} r^{-3/2}$, and $\omega_{0\ell}$ are the f -mode angular frequencies of the NS, where the subscript 0 indicates that the mode amplitude has no radial nodes. The

quantity $\mathcal{Q}_{\ell m}$ is

$$\mathcal{Q}_{\ell m} = \cos(\Omega \hat{t}^2) \left[1 + 2 \text{F}_S \left(\frac{\sqrt{3}}{2\sqrt{\pi}} \hat{t} \right) \right] - \sin(\Omega \hat{t}^2) \left[1 + 2 \text{F}_C \left(\frac{\sqrt{3}}{2\sqrt{\pi}} \hat{t} \right) \right], \quad (12)$$

where the functions F_S and F_C are Fresnel sine and cosine integrals respectively using the conventions in Mathematica. We have defined

$$\hat{t} = \frac{8}{5\sqrt{\epsilon_m}} \left(1 - \frac{r^{5/2} \omega_{0\ell}^{5/3}}{m^{5/3} M^{5/6}} \right), \quad (13)$$

and

$$\epsilon_m = \frac{256\mu M^{2/3} \omega_{0\ell}^{5/3}}{5m^{5/3}}. \quad (14)$$

In Eq. (11) a body label A, B on the quantities $\omega_{0\ell}$, \hat{t} , ϵ_m , and $\mathcal{Q}_{\ell m}$ is implied. For each ℓ -multipole only $m = \ell$ contributes in Eq. (11) because the effect of modes with $m < \ell$ has already been taken into account as adiabatic contributions. For the lowest order multipoles the coefficients are given by $(a_2, a_3, a_4) = (\frac{1}{4}, \frac{3}{8}, \frac{29}{64})$ and $(b_2, b_3, b_4) = (\frac{3}{4}, \frac{5}{8}, \frac{35}{64})$.

Similar to the treatment for the conservative dynamics, the effect of dynamic f -mode tides can be incorporated in the dissipative sector in an approximate way by multiplying the occurrences of k_ℓ in $h_{\ell m}^{\text{tidal}}$ in Eq. (10) by an effective function $k_\ell \rightarrow k_\ell \hat{k}_{\ell \text{ dyn}}^{\text{diss}}$. For $\ell = 2$ this function is given by

$$\hat{k}_{2 \text{ dyn}}^{(A) \text{ diss}} = \frac{\hat{k}_{2 \text{ dyn}}^{(A)} (\omega_{0\ell}^2 + 6X_B \Omega^2)}{3\Omega^2 (1 + 2X_B)}, \quad (15)$$

where $\hat{k}_{2 \text{ dyn}}^{(A)}$ is the enhancement function for body A in the conservative dynamics from Eq. (11). We find that similar factors for other modes and from higher multipoles have only a small impact on the results and therefore neglect them in this study; they are further discussed in Ref. [62].

C. Adiabatic tides with Gravitational Self-Force-inspired potential: $\text{EOB}_{\text{adGSF+}}$

Gravitational self-force calculations have recently computed tidal invariants that contain information about strong-field tidal effects in the limit of small mass ratios, to linear order in X_A [45, 63]. These results have been augmented in Ref. [45, 46] by a term $\propto X_A^2$ that would describe currently unknown second-order self-force effects. Specifically, in this model Eq. (7) is employed with the

potential $\hat{A}^{(A)}$ given by

$$\hat{A}_{\text{adGSF+}}^{(A)} = 1 + \frac{3u^2}{(1 - r_{\text{LR}}u)} + X_A \frac{a_1^{\text{GSF}}(u)}{(1 - r_{\text{LR}}u)^{7/2}} + X_A^2 \frac{a_2^{\text{GSF}}(u)}{(1 - r_{\text{LR}}u)^p} + (1 \leftrightarrow 2) \quad (16)$$

The caveats with the choice of gauge for mapping GSF results to EOB potentials that contain explicit poles at the light ring r_{LR} are discussed in [48]. In Eq. (16), the coefficient $a_1^{\text{GSF}}(u)$ is obtained from Eqs. (7.24)–(7.27) of Ref. [45]. In the model of Ref. [46] the unknown parameter a_2^{GSF} is set to $a_2^{\text{GSF}}(u) = 337u^2/28$ and the unknown exponent p is chosen to be $p = 4$. The radius of the light ring r_{LR} is obtained from the conservative EOB dynamics by solving

$$\tilde{A}(r_{\text{LR}}) - \frac{r_{\text{LR}}}{2} \tilde{A}'(r_{\text{LR}}) = 0, \quad (17)$$

with the potential $\tilde{A} = A_{\text{pp}} + A_{\text{adPN}}^{\text{tidal}}$ from the PN model in Eqs. (7) and (9).

For tests involving the $\text{EOB}_{\text{adGSF+}}$ model we use the publicly available code of [57] that was also used to create the surrogate model in [64]. Note that this code differs from the EOB model described above in the point-particle sector: (i) non-quasi-circular (NQC) corrections (the factor $N_{\ell m}$ in the waveform modes of Eq. (6) that is necessary to accurately describe the BBH merger) are omitted, (ii) a different resummation of the potentials A_{pp} and D is used, (iii) the arguments of factors in $h_{\ell m}^{\text{F}}$ such as $\rho_{\ell m}$ involve powers of $v_\phi = (\partial H_{\text{EOB}}/\partial p_\phi)^{-2/3} \Omega$ evaluated for circular orbits instead of $v = \Omega^{1/3}$, (iv) the higher-order logarithms in the tail terms are Padé-resummed, and (v) the calibration of the BBH model is different. The influence of these differences play only a marginal role compared to the tidal effects and how those are incorporated in the EOB model, therefore, we will present results obtained with [57] for $\text{EOB}_{\text{adGSF+}}$. However, more details about the influence of the underlying point mass models will be given in Appendix C.

III. BINARY CONFIGURATIONS AND NUMERICAL METHODS

In this work we consider eight different configurations that have already been studied in [56] with lower resolution. The initial configurations are constructed with SGRID, see [54, 65, 66] for detailed descriptions. Dynamical evolutions are performed with the BAM code, see e.g. [67–69].

We choose two zero-temperature EOSs modeled by piecewise polytropes [70]: SLy [71] and MS1b [72]. The EOSs are chosen to cover a large range in the BNS parameter space with respect to the tidal coupling constant

$$\kappa_2^T := 2 \left(\frac{q^4}{(1+q)^5} \frac{k_2^A}{C_A^5} + \frac{q}{(1+q)^5} \frac{k_2^B}{C_B^5} \right), \quad (18)$$

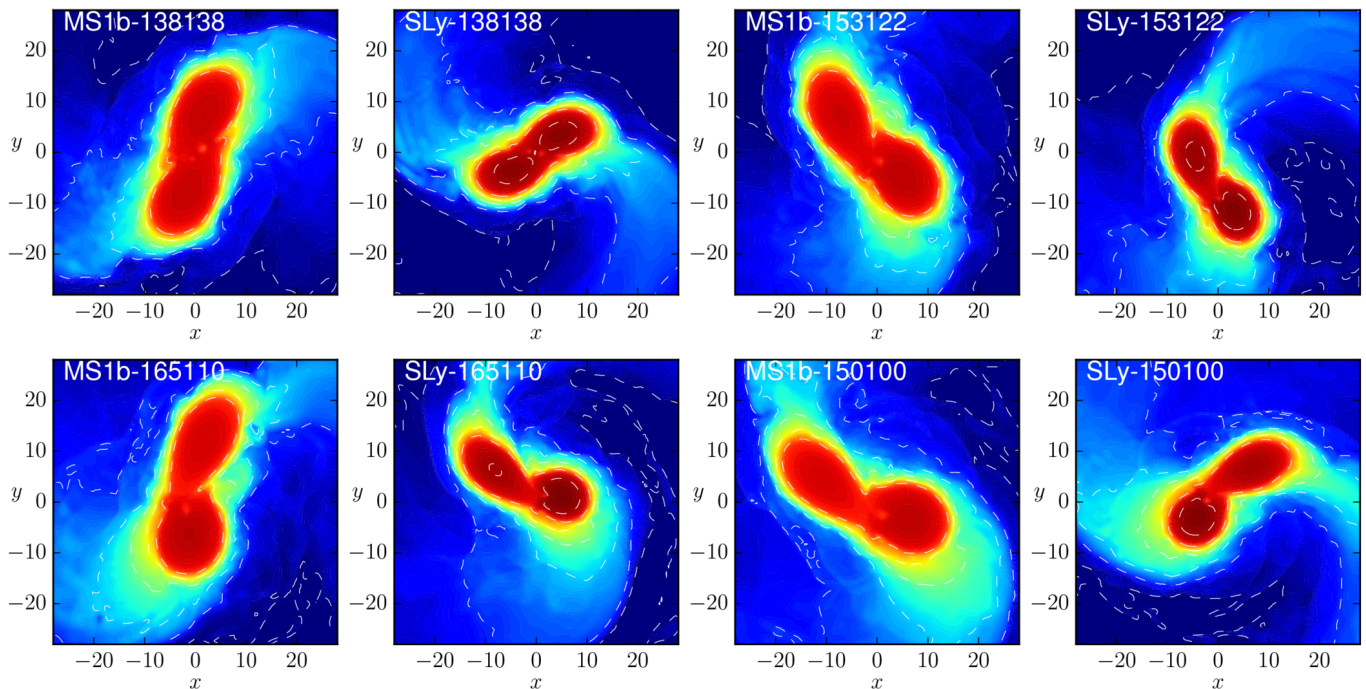


FIG. 1: Density profile of the setups we investigate (resolution R3). The rest-mass density ρ is shown for all panels on a color bar ranging from $10^{-9} \simeq 6.2 \cdot 10^8 [\text{g}/\text{cm}^3]$ (dark blue) to $10^{-2.8} \simeq 9.8 \cdot 10^{14} [\text{g}/\text{cm}^3]$ (dark red). White dashed lines correspond to values of the density of $10^{-9}, 10^{-8}, 10^{-7}, 10^{-6}, 10^{-5}, 10^{-4}, 10^{-3}$. The x - y -range is the same in all panels. The plots illustrate that (i) the inner region of the NSs is less dense for stiffer EOSs; (ii) the NS radii are larger for stiffer EOSs; (iii) the tidal deformation of the lower mass constituent increases with increasing mass ratio; (iv) the NSs come into contact before the actual merger (peak in GW amplitude).

which characterizes Newtonian tidal effects in the EOB Hamiltonian. For the dynamical evolution we add an additional component to the pressure to describe thermal effects $p_{\text{th}} = \epsilon\rho(\Gamma_{\text{th}} - 1)$ with $\Gamma_{\text{th}} = 1.75$ [73]. For both EOSs we focus on four different setups defined by their total mass

$$M = M^A + M^B \quad (19)$$

and their mass ratio

$$q = M^A/M^B. \quad (20)$$

The parameters for our setups are $(M, q) = (2.75, 1.0), (2.75, 1.25), (2.75, 1.50), (2.50, 1.50)$. To illustrate the effect of changes in the parameters on the merger process we show in Fig. 1 the 2D density snapshots of these systems at merger, which corresponds to the peak in the GW amplitude. The density snapshots are gauge-dependent quantities, therefore, Fig. 1 enables only a qualitative interpretation.

Building on results from our previous work [56], we have performed new simulations of the setups at higher resolution. Thus, three different resolutions denoted by (R1,R2,R3) are available for each configuration. The resolutions on the finest grid covering the NSs are $(0.23, 0.15, 0.12)$ for the SLy setups and $(0.25, 0.16, 0.13)$ for MS1b. With these resolutions the diameters of the stars are covered by approx. 64, 96, and 128 grid points,

respectively. Details about the configurations are given in Tab. I.

To compute results for the periastron advance we consider as a representative case the setup MS1b-150100. Reliably extracting this information from NR data, as described in Appendix A, requires an additional simulation with higher eccentricity that we perform following the approach of [56, 74].

IV. DYNAMICS

To study the dynamics and energetics of BNS mergers, we present results for the binding energy vs. orbital angular momentum of the binary. They were proposed as important diagnostic tools to assess the performance of EOB models in [75] and were later applied for BNS systems in [76].

A. Binding energy curves in the EOB model

For the binding energy curves we evaluate

$$E = (H_{\text{EOB}} - M)/\mu \quad (21)$$

and

$$\ell = p_\phi \quad (22)$$

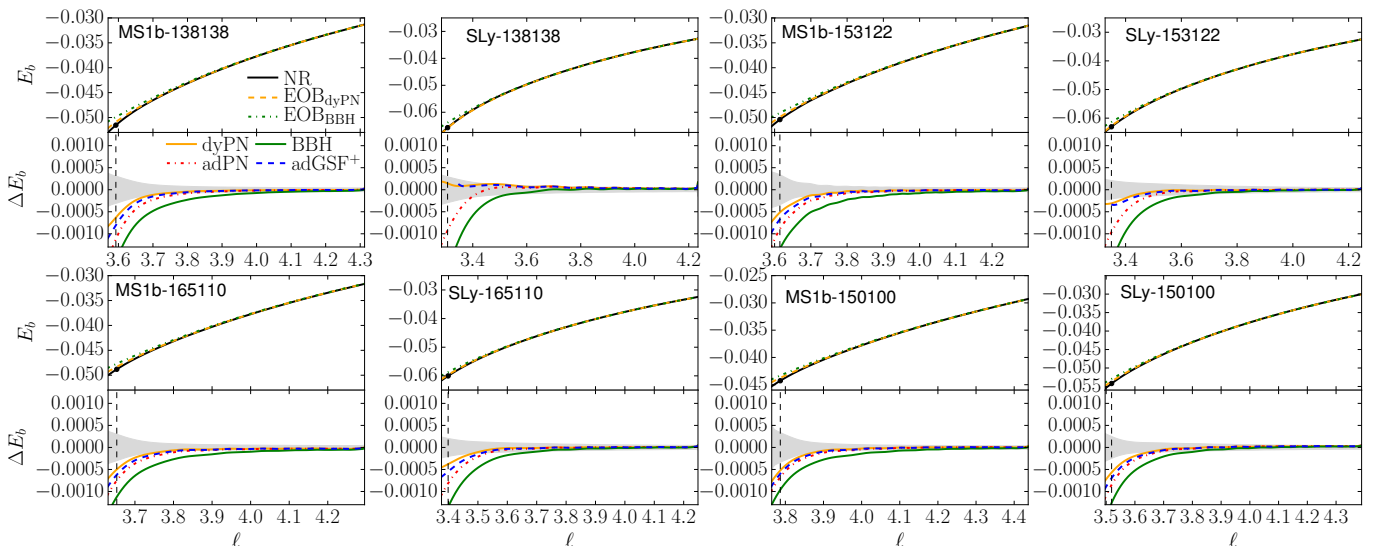


FIG. 2: Binding energy E vs. orbital angular momentum ℓ curves. The name of the configuration is shown in the upper left hand corner of the corresponding panel. Upper panels: $E(\ell)$ curves for setups with R3 resolution. We include the EOB estimates EOB_{BBH} (green) and EOB_{dyPN} (orange). The moment of merger of the NR results is shown as a circle. Bottom panels: Difference between the EOB results and the NR data. The moment of the NR merger is marked as a vertical black dashed line. The shaded region is the numerical uncertainty estimated from Eq. (27). The ordering of the panels is identical to Fig. 1.

using the solutions to the evolution equations for (r, p_{r^*}, p_ϕ) and obtain the results parametrically.

B. NR error budget

We compute the dimensionless binding energy and angular momentum per reduced mass as

$$E = [(M_{\text{ADM}}(t=0) - \mathcal{E}_{\text{rad}})/M - 1] \nu^{-1}, \quad (23)$$

$$\ell = (J_{\text{ADM}}(t=0) - \mathcal{J}_{\text{rad}})(M^2 \nu)^{-1}, \quad (24)$$

respectively. Here, M_{ADM} and J_{ADM} describe the ADM-mass and ADM-angular momentum, and \mathcal{E}_{rad} and \mathcal{J}_{rad} are the energy and angular momentum emitted from the system via GWs. The radiated energy and angular momentum perpendicular to the orbital plane are calculated as

$$\mathcal{E}_{\text{rad}} = \frac{1}{16\pi} \sum_{l,m} \int_0^t dt' \left| r \dot{h}_{lm}(t') \right|^2, \quad (25)$$

$$\mathcal{J}_{z \text{ rad}} = \frac{1}{16\pi} \sum_{l,m} \int_0^t dt' m \left[r^2 h_{lm}(t') \dot{h}_{lm}^*(t') \right], \quad (26)$$

with $l_{\text{max}} = 8$.

The binding energy vs. orbital angular momentum curves are directly accessible from our numerical simulations, i.e. no alignment or additional shift is needed. This makes $E(\ell)$ curves an unambiguous and effective tool for a comparisons with analytical models.

To assess the uncertainty of $E(\ell)$ for our simulations we consider four different sources of error:

- (i) *Uncertainty of the binding energy at $t = 0$.* Because of the limited number of points in SGRID and the interpolation of the SGRID initial data on the BAM grid, the initial ADM-mass as well as the individual component masses are only accurate up to $\sim 10^{-5}$. We account for this uncertainty through $\Delta E_{\Delta M} = 2 \times 10^{-5}$.
- (ii) *Uncertainty of the angular momentum at $t = 0$.* Similar to the ADM mass, the angular momentum also contains numerical uncertainties of the order of $\Delta J_{\text{ADM}}(t) \sim 10^{-3}$. This leads to $\Delta \ell(t=0) = \Delta J_{\text{ADM}}(t=0)/(M^A M^B) \sim 10^{-3}$, where we estimate the uncertainty conservatively as $\Delta \ell = 2 \times 10^{-3}$. Since $\Delta \ell$ leads to a horizontal shift in the $E(\ell)$ curve we assign a time dependent error on the binding energy of $\Delta E_{\Delta J}(\ell) = E(\ell) - E(\ell - \Delta \ell)$.
- (iii) *Finite radius extraction effects.* Another source of error is caused by the finite size of computational domain and the finite extraction radii. As shown in [32] this error is small ($\lesssim 10^{-1}$ rad). To estimate the resulting uncertainty we use two extraction radii, $r_1 = 1000M$ and $r_2 = 750M$, and compute the difference in $E(\ell)$, i.e. $\Delta E_r(\ell) = E_{r_1}(\ell) - E_{r_2}(\ell)$. In future work with more accurate NR data the waveform has to be extrapolated to infinity, but for the scope of this paper 20170207 the simple estimate is sufficient.
- (iv) *Numerical discretization.* We estimate this error by considering different resolutions. As shown in [26, 32] a conservative error estimate for the

triplet of resolutions employed in this article is to compute the difference between resolution R3 and R2 $\Delta E_{\Delta x}(\ell) = E_{R3}(\ell) - E_{R2}(\ell)$. We find that $\Delta E_{\Delta x}(\ell)$ dominates the overall error in most cases.

The total uncertainty of the numerical data is approximated by

$$\Delta E_{NR}(\ell) = \sqrt{\Delta E_{\Delta M}^2 + \Delta E_{\Delta J}^2(\ell) + \Delta E_r^2(\ell) + \Delta E_{\Delta x}^2(\ell)}. \quad (27)$$

C. Results for $E(\ell)$

1. General features

Our results are summarized in Fig. 2, where $E(\ell)$ is shown for the NR data (black), the EOB_{BBH} model (green), and the EOB_{dyPN} model (orange) in the top panels and the difference between the NR results and the EOB models in the bottom panels. The ordering of the panels is the same as in Fig. 1.

To aid in the interpretation of our results we first discuss important general aspects of the $E(\ell)$ curves. Because of the attractive nature of tidal effects BNS systems are more bound than BBH systems once systems with the same specific angular momentum are compared. Consequently, the binding energy for a given angular momentum is smaller for BNS setups than for the corresponding BBH case ².

The influence of the EOS on $E(\ell)$ is deduced by contrasting the MS1b and SLy curves in adjacent panels of Fig. 2. We observe that for stiffer EOS (MS1b) the merger occurs at larger orbital angular momentum and larger binding energy, so the merger remnant is less bound for MS1b than for SLy. This effect is also visible in Fig. 1, where MS1b setups merge at larger distances because of their lower compactness. The influence of the mass ratio is illustrated in Fig. 2 by comparing panels with the same EOS (but excluding the 150100 setups that have a lower total mass). We see that for increasing mass ratio the moment of merger also occurs at higher binding energy and angular momentum. Finally, the bottom panels with the same EOS in Fig. 2 show that an increase in the total mass of the system also leads to a more bound merger remnant. Most of these findings can be explained by the quasi-universal properties of BNS mergers reported in [78–80] and the influence of κ_2^T on the inspiral and merger dynamics.

2. EOB-NR comparison

Comparing the EOB and NR curves in Fig. 2 shows that for most setups the tidal EOB models deviate from the NR predictions shortly before merger. This disagreement between NR and EOB is larger for stiffer EOSs, smaller total masses, and higher mass ratios, i.e. setups with larger tidal effects. Furthermore, it is evident that for all simulations EOB_{dyPN} and $\text{EOB}_{\text{adGSF+}}$ stay closer to the NR result than EOB_{adPN} . This observation is independent of the EOS, mass, and mass ratio. The origin of the larger tidal effects for EOB_{dyPN} and $\text{EOB}_{\text{adGSF+}}$ compared to EOB_{adPN} is different for each model: for EOB_{dyPN} the dynamical tides enlarge k_ℓ when the orbital frequency approaches the resonance frequency of the individual stars, while enhanced tides for $\text{EOB}_{\text{adGSF+}}$ are caused by approaching the light ring in the GSF^+ -potential, Eq. (16).

Another interesting aspect is the location of the merger point of the individual models: except for the $\text{EOB}_{\text{adGSF+}}$ model in the cases SLy-138138 and SLy-153122 (where the $\text{EOB}_{\text{adGSF+}}$ merger corresponds to the endpoint of the blue dashed curve) the merger for all EOB models occurs at smaller angular momentum and binding energy than in the NR simulations. This is interesting since it shows that in most cases the final merger remnant is less bound than predicted by the EOB models and that additional repulsive effects that are not included in the current EOB description become important near merger.

We emphasize that the NR error quoted here is chosen conservatively, i.e., deviations between the NR and the EOB results outside the NR error bars mark region where the EOB models must be further improved. But note that due to numerical dissipation, which acts as an artificially attractive force, the continuum solution will have smaller tidal effects than the NR results presented here and will therefore be closer to the EOB models. Thus, the correct solution will lie within the lower part of the shaded regions in the bottom panels of Fig. 2.

V. PERIASTRON ADVANCE

A. Periastron Advance in the EOB models

The PA is characterized by the ratio of angular and radial frequencies $K = \Omega_\phi/\Omega_r$ and, in the case considered here, is influenced by a combination of relativistic and tidal effects. In the limit of circular orbits, as discussed e.g. in [81, 82], the PA for nonspinning binaries and for the classes of tidal models considered here can be computed from

$$K^{-2} = D^{-1} \left[A \left(3 + \frac{rA''}{A'} \right) - 2rA' \right], \quad (28)$$

² Note that for systems with the same frequency the opposite statement holds, i.e., the binding energy at a given frequency is larger for BBHs than for BNSs see the description in [77].

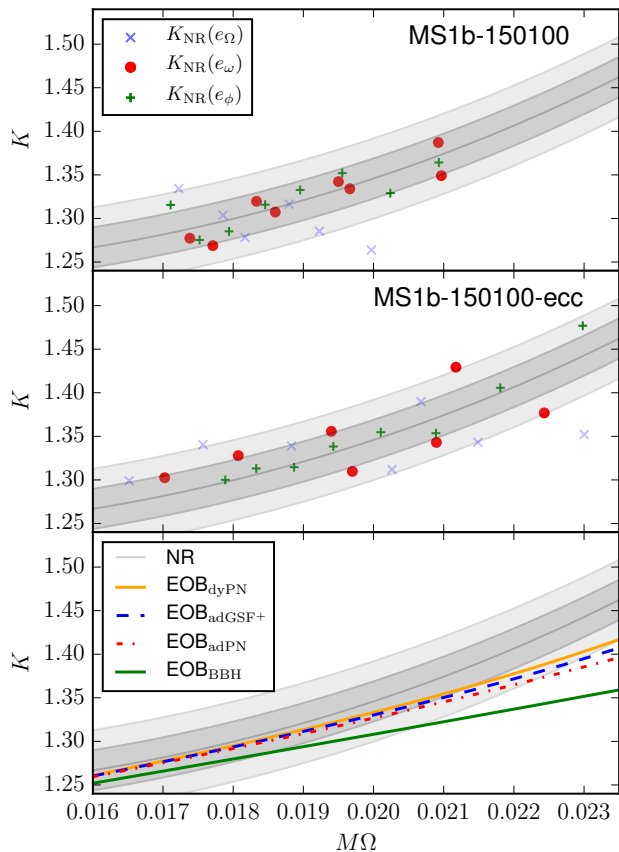


FIG. 3: The top panel shows the NR results for setup MS1b-150100. Different markers represent results obtained for different eccentricity estimates. The middle panel represents the results for configuration MS1b-150100-ecc. The bottom panel shows the PA for the NR data and all EOB models. The NR data are obtained from a fit to the results $K_{\text{NR}}(e_\omega)$, $K_{\text{NR}}(e_\phi)$. The shaded intervals mark the 1σ and 2σ region of the fit.

B. Extracting the Periastron Advance from NR Simulations

The computation of the PA for NR simulations relies on a suitable indicator for the eccentricity. In this work, we test three different indicators e_Ω , e_ω , e_ϕ based on the orbital frequency Ω , the GW frequency of the (2,2)-mode ω_{22} , and the GW phase ϕ_{22} of the (2,2)-mode. A detailed description is given in Appendix A.

From the eccentricity indicator we calculate the PA following the work of [83]. We determine the times t_k of the extrema of e corresponding to perihelia and aphelia and compute the orbital phase ϕ_Ω and GW phase ϕ_{22} at these times t_k . Finally the ratio between the angular and radial frequency is given by

$$K = \frac{\Omega_\phi}{\Omega_r}(t_k) = \frac{\phi_\Omega(t_{k+1}) - \phi_\Omega(t_k)}{2\pi} = \frac{\phi_{22}(t_{k+1}) - \phi_{22}(t_k)}{4\pi}, \quad (29)$$

where each equal sign corresponds to a different way of extracting K from the NR data.

C. EOB-NR comparison

Extracting K from NR simulations is only possible for sufficiently long inspirals. Furthermore, as shown in e.g. [83], it is difficult to determine K for simulations with almost vanishing eccentricity. For these reasons we focus on the MS1b-150100 setup which has the lowest starting frequency. Further we perform a new simulation with higher eccentricity: MS1b-150100-ecc.

Figure 3 shows K for all eccentricity measurements for MS1b-150100 in the upper panel, and the results for MS1b-150100-ecc in the middle panel³. We find that the scattering of data points obtained from $K_{\text{NR}}(e_\phi)$ is smallest and that these results are in agreement with $K_{\text{NR}}(e_\omega)$. By contrast the results from $K_{\text{NR}}(e_\Omega)$ are more scattered and do not help to put constraints on K . Thus, we combine all data points obtained with $K_{\text{NR}}(e_\phi)$ and $K_{\text{NR}}(e_\omega)$ and fit the NR data for both configurations according to

$$K_{\text{NR}}(M\Omega) = \frac{c_0 + c_1(M\Omega) + c_2(M\Omega)^2}{\sqrt{1 - 6(M\Omega)^{\frac{2}{3}}}}, \quad (30)$$

cf. [82]. We indicate the 1σ and 2σ region of the fit as dark and light shaded regions respectively in Fig. 3.

The bottom panel of Fig. 3 illustrates that the NR data contains larger tidal effects than those predicted by the EOB models. Because of the difficulties in reliably computing the NR error for the PA (as discussed in Appendix A, see also [82] for uncertainty estimates of PA in BBH setups) the results presented here have to be considered with caution. However, it is clearly visible from Fig. 3 that for low frequencies $M\Omega < 0.019$ the PA predicted from the EOB models and the results from the NR simulations agree very well, cf. dark shaded region. At higher frequencies the curves start to deviate and the point-mass result EOB_{BBH} becomes distinguishable from the NR uncertainty region. The EOB_{BBH} result leaves the 1σ region at $M\Omega \approx 0.019$ and the 2σ region at $M\Omega \approx 0.021$. This demonstrates for the first time that current NR simulations are able to resolve tidal effects on the PA. Up to frequencies of order $M\Omega \approx 0.023$ the results from the EOB models EOB_{dyPN} and $\text{EOB}_{\text{adGSF+}}$ remain within the 2σ region of the NR data. Beyond this frequency no additional NR data points (see upper and middle panel) are available and, thus, no further statement to discriminate between different tidal EOB models can be made.

³ We have simulated MS1b-150100-ecc only for resolution R1. The resolution has only a small influence on the measurement of the PA, since resolution effects become dominant at later times of the simulation, where no eccentricity can be measured at all.

VI. WAVEFORMS

A. EOB waveforms

The EOB waveforms are computed by evaluating the functions $h_{\ell m}^F$ in Eq. (10). They depend on the EOB trajectory and enter into the backreaction of GW losses on the dynamics through Eq. (4). To compute the time evolution of the modes we therefore solve the algebraic equations (10) jointly with the EOB equations of motion.

B. NR error budget

Gravitational waves are extracted using the Newman-Penrose formalism [84] from the curvature scalar Ψ_4 . Individual modes can be obtained by a multipole decomposition on extraction spheres using spherical harmonics with spin weight -2 . The algorithm and implementation is described in detail in [67]. We reconstruct the metric multipoles $r h_{lm}$ from the curvature multipoles $r \Psi_4^{lm}$ using the frequency domain integration of [85] with a cutting frequency of $m\omega_{22}^0/2$, see Tab. I.

1. $\phi(t)$ -Evolution

The NR waveforms are presented as a function of the retarded time

$$u = t - r_* = t - r_{\text{extr}} - 2M \ln[r_{\text{extr}}/(2M) - 1]. \quad (31)$$

For the extraction radius we use the value $r_{\text{extr}} = 1000$. As shown in [32] for this radius the error due to using waveforms extracted at a finite radius is of order ~ 0.1 rad and decreases during the simulation because the GW frequency increases. As a simple error estimate we compute $\Delta\phi_r = \phi_{r_1} - \phi_{r_2}$ with $r_1 = 1000$ and $r_2 = 750$, similar to the investigation of the binding energy discussed above.

In most simulations the dominant source of uncertainty are truncation errors during the last few orbits before merger. We estimate the uncertainty due to finite resolution by the difference between setups R3 and R2, $\Delta\phi_{\Delta x} = \phi_{R3} - \phi_{R2}$. As shown in [26, 32] for these resolutions this is a conservative measure of the error.

Finally, we also take into account that mass is not exactly conserved in the simulations. In particular, as discussed in [69], the treatment of the atmosphere can cause mass loss or gain and is a source of systematic errors. The dephasing caused by variations in the mass is taken into account as $\Delta\phi_{\Delta M} = \omega u \Delta M_b / M_b$, where M_b denotes the baryonic mass of the system at the beginning of the simulation and ΔM_b is the change in the baryonic mass.

The total phase uncertainty is then given by

$$\Delta\phi = \max_{\tilde{u} \in [0, u]} \sqrt{\Delta\phi_r^2(\tilde{u}) + \Delta\phi_{\Delta x}^2(\tilde{u}) + \Delta\phi_{\Delta M}^2(\tilde{u})}. \quad (32)$$

We take into account that some errors are non-monotonic by using $\max_{\tilde{u} \in [0, u]}[\dots]$. This ensures that the total error is always increasing over time ⁴.

2. $\phi(\omega)$ -Evolution

In addition to the time evolution of the GW phase, we also present the phase accumulated over a given frequency interval. For all setups we compute the accumulated phase with respect to the reference frequency $M\omega_{22} = 0.04$, which corresponds to 470Hz for $M = 2.75$ and to 517Hz for $M = 2.50$. The details of the computation are discussed in Appendix B.

The error budget of $\phi(\omega)$ contains the following components, similar to the analysis of the time evolution $\phi(t)$:

- (i) We take into account the fact that the GWs are extracted at finite radii by considering $\Delta\phi_r(\omega) = \phi_{r_1}(\omega) - \phi_{r_2}(\omega)$ with $r_1 = 1000$ and $r_2 = 750$.
- (ii) The uncertainty caused by numerical discretization is estimated as $\Delta\phi_{\Delta x}(\omega) = \phi_{R3}(\omega) - \phi_{R2}(\omega)$.
- (iii) We include an estimate resulting from the non-conservation of the total mass $\Delta\phi_{\Delta M}(\omega)$.
- (iv) An additional source of error is the uncertainty caused by the low-pass filtering of the raw NR data (Appendix B). We account for this by varying the cutoff-frequency by a factor of 2 and obtain the estimate $\Delta\phi_{\Delta\omega_{\text{cut}}}(\omega) = \phi_{\omega_{\text{cut}}}(\omega) - \phi_{2\cdot\omega_{\text{cut}}}(\omega)$.
- (v) A further contribution to the error budget arises from the fact that the phase evolution is computed with respect to a phase at $M\tilde{\omega}_{22} = 0.04$. The uncertainty in this reference value is estimated to be $\Delta\phi_{M\tilde{\omega}}(\omega) = \phi_{M\tilde{\omega}}(\omega) - \phi_{M\tilde{\omega} \pm 2.5 \times 10^{-4}}(\omega)$.

The total error is given as:

$$\Delta\phi(\omega) = \left[\Delta\phi_r^2(\omega) + \Delta\phi_{\Delta x}^2(\omega) + \Delta\phi_{\Delta M}^2(\omega) + \Delta\phi_{\Delta\omega_{\text{cut}}}^2(\omega) + \Delta\phi_{M\tilde{\omega}}^2(\omega) \right]^{1/2}. \quad (33)$$

C. EOB-NR comparison: $\phi(t)$

As shown in e.g. [56] more than 99% of the total energy emitted in a BNS merger up to a mass ratio of $q = 1.5$ is contained in the (2,2) mode. This motivated previous EOB and NR comparisons to focus solely on this mode.

⁴ Note that we do not include the influence of the residual eccentricity in our error budget since this would require the use of eccentricity reduced waveforms. But as presented in [54] the remaining eccentricity can cause phase differences of the order of ~ 0.2 rad.

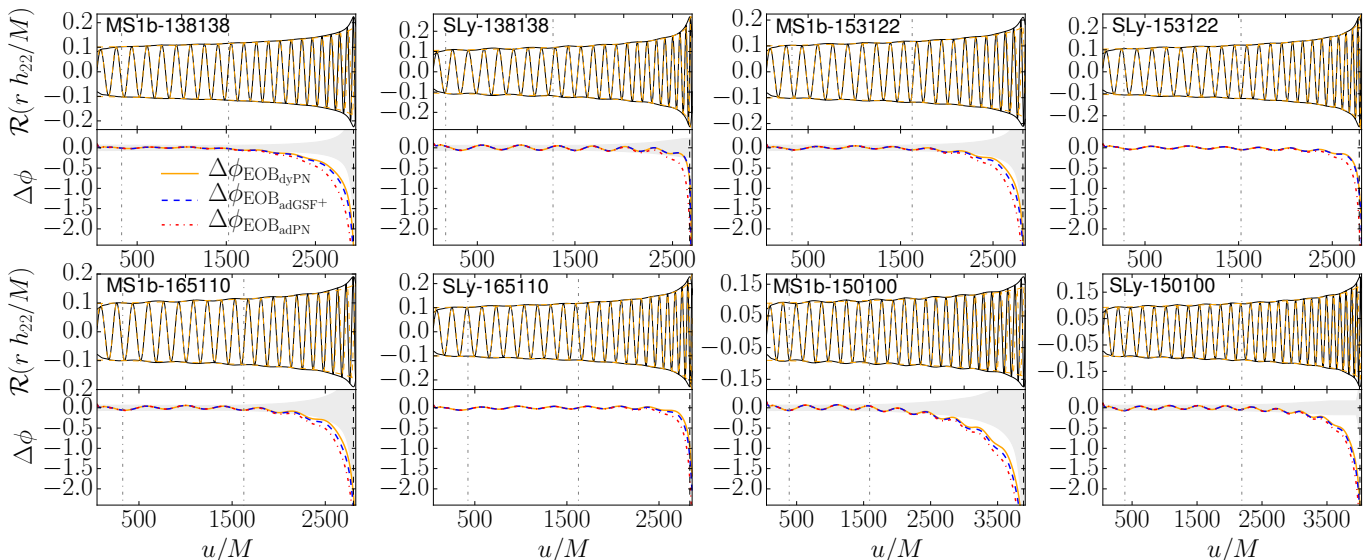


FIG. 4: Dominant (2,2)-mode of the GW for all configurations. The top panels represent the real part and the amplitude of the NR data (black) and the EOB_{dyPN} model (orange). The vertical dash-dotted lines show the interval over which the EOB and NR waveform are aligned. The bottom panels represent the dephasing $\Delta\phi = \phi_{\text{EOB}} - \phi_{\text{NR}}$ in rads for the tidal EOB models. The shaded region represents the estimate of the uncertainty in the NR results, and the vertical dashed line marks the moment of merger from NR. Notice that the ordering of the panels is identical to Fig. 1.

However, we want to go beyond previous work and include the (2,1), (3,3), and (4,4) mode in our comparison.

By contrast to the comparisons of results for $E(\ell)$, K , and $\phi(\omega)$ discussed below, we do not include the EOB_{BBH} model in our analysis of $\phi(t)$. The reason is that a robust comparison of the dephasing over time requires aligning two waveforms over a time interval where they agree. However, our simulations cover only the last ~ 10 orbits before merger, where tidal effects *cannot* be neglected and a reliable alignment of BBH and BNS waveforms cannot be achieved.

1. Dominant (2,2)-mode

Figure 4 presents the results for the time evolution of the dominant (2,2)-mode. In the upper panels the real part of rh_{22} is shown for the NR data (black) and the EOB_{dyPN} model (orange dashed), we also include the amplitude $|rh_{22}|$ as thin lines. The time interval used for the alignment is marked by vertical gray dash-dotted lines⁵. In the bottom panel we present the difference between the NR waveform and the tidal EOB models. The moment of merger in the NR simulation is shown as a vertical black dashed line in the bottom panels. The numerical uncertainty is shown as a shaded region.

We conclude from Fig. 4 that:

- (i) For setups with a small tidal coupling constant the dephasing between EOB and NR waveforms is small and remains within the numerical uncertainty almost up to the merger.
- (ii) Variations in the mass ratio have a negligible effect on the performance of the EOB models when considering $\phi(t)$.
- (iii) For setups with stiffer EOSs the EOB models start to deviate from the NR simulation a few orbits before the merger.
- (iv) In all cases the EOB models underpredict tidal effects, i.e. $\phi_{\text{EOB}}(u) < \phi_{\text{NR}}(u)$.
- (v) The EOB merger generally occurs after the NR merger.
- (vi) For all setups the performance of the tidal EOB models is similar, with the EOB_{dyPN} and $\text{EOB}_{\text{adGSF+}}$ models remaining closer to the NR results than the EOB_{adPN} model.

2. Higher modes

While for equal mass configurations the (2,1) and (3,3) modes are zero, they are non-zero for unequal masses. The energy emitted in the (2,1) and (3,3) mode increases almost linearly for an increasing mass ratio. By contrast the amplitude and consequently the emitted energy of the (4,4) mode is almost independent of the mass ratio, see [56] for further details. We present the (4,4) mode

⁵ For large κ_2^T changing the alignment interval effects $\Delta\phi(t)$ and a more robust comparison would require longer NR simulations.

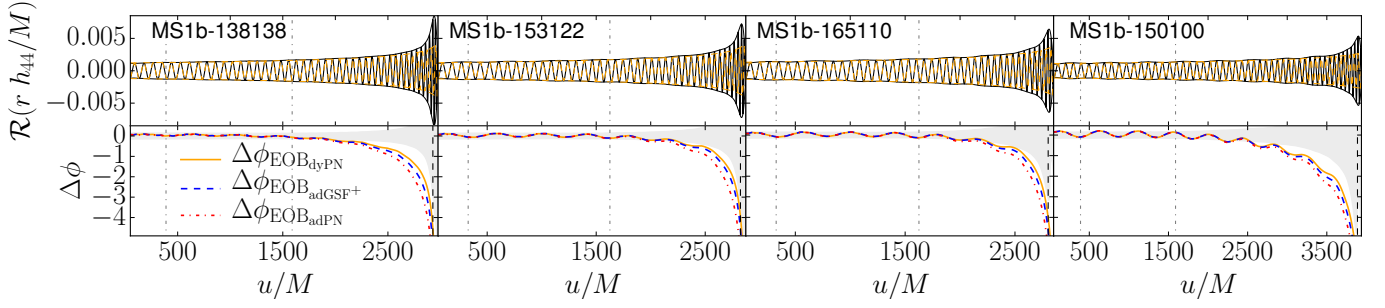


FIG. 5: (4,4)-mode of the GW for MS1b configurations. The top panels represent the real part and the amplitude of the NR data (black) and the EOB_{dyPN} model (orange). The vertical dash-dotted lines show the interval used to align the EOB and NR waveform. The bottom panels represent the dephasing $\Delta\phi = \phi_{\text{EOB}} - \phi_{\text{NR}}$ in rads for the tidal EOB models. The shaded region represents the estimate of the uncertainty of the NR results. The vertical dashed line marks the moment of merger for the NR result.

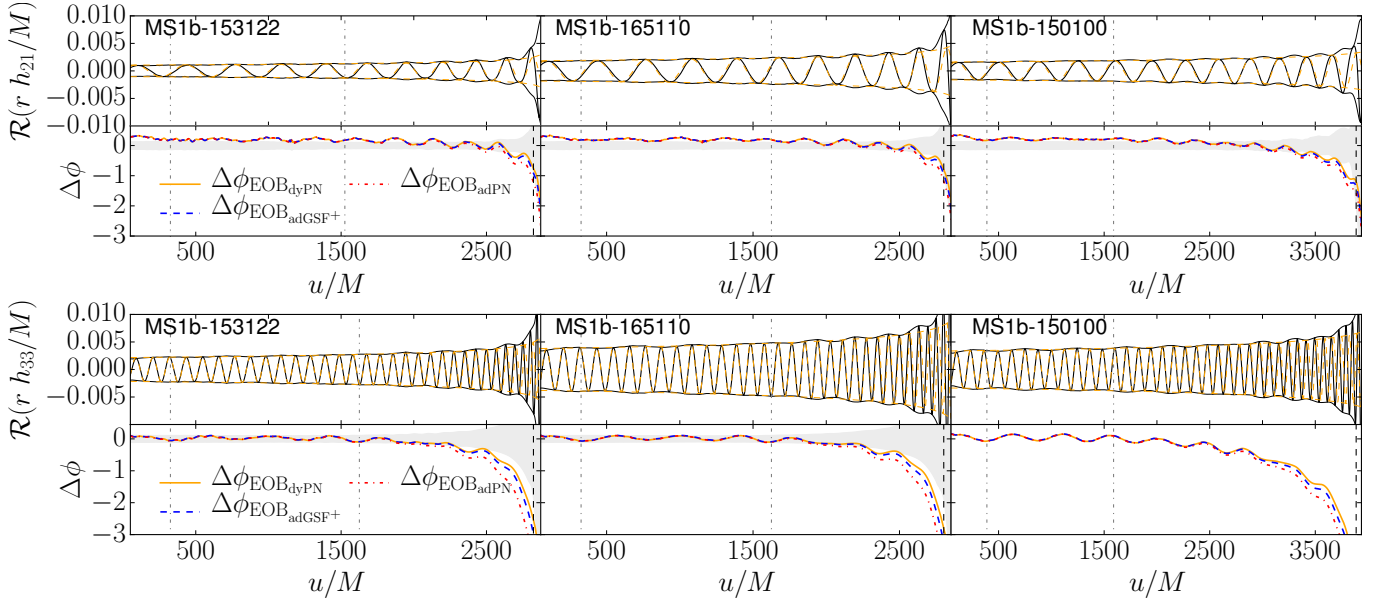


FIG. 6: (2,1)-mode (top panels) and (3,3)-mode (bottom panels) of the GW signal for the unequal mass setups employing the MS1b EOS. The top panels represent the real part and the amplitude of the NR data (black) and the EOB_{dyPN} model (orange). The vertical dash-dotted lines show the interval used to align the EOB and NR waveform. The bottom panels represent the dephasing $\Delta\phi = \phi_{\text{EOB}} - \phi_{\text{NR}}$ for the different tidal EOB models in rads. The shaded region represents the estimate of the uncertainty of the NR results. The vertical dashed line marks the moment of merger for the NR result.

for all models employing the MS1b EOS in Fig. 5⁶. The (2,1) and (3,3) mode for the unequal mass setups with MS1b EOS are shown in Fig. 6. We used the alignment based on the (2,2) mode, where we obtained the time and phase shifts $(\delta t^{\text{align}}, \delta\phi_{22}^{\text{align}})$. This determines the shifts for the other (ℓ, m) modes to be $\delta\phi_{\ell m}^{\text{align}} = m\delta\phi_{22}^{\text{align}}/2$, together with the same time shift. Another consideration is that the point-mass EOB model for higher modes has not been calibrated to NR results, e.g. there is no

equivalent function to N_{22} . As shown in Appendix C, the influence of such calibrations of the EOB model is $\lesssim 0.03\text{rad}$ for the MS1b setups and thus much smaller than the size of tidal effects.

Overall we find that the dephasing for the higher modes is similar to the results obtained for the dominant (2,2) mode. The performance of the EOB models depends only weakly on the mass ratio since q has only a small influence on the tidal coupling constant. By contrast, the total mass impacts the accuracy of the EOB models since tidal effects strongly decrease with increasing total mass. For example, for MS1b-150100 where κ_2^T is ~ 180 larger than for MS1b-165110 the dephasing from NR is larger since the larger tidal effects are inadequately captured by the models.

⁶ Note that we do not study systems employing the SLy EOS since those have (as presented in [56]) a larger drift of the center of mass, which effects the computation of the subdominant modes.

Considering the agreement of the amplitude between the EOB models and the NR results, we find that close to the moment of merger the amplitude predicted by the EOB model is smaller than those for the NR simulation. This is true for all setups and is a robust (qualitative) observation. However, since the computation of the subdominant modes is challenging and the numerical simulations are more inaccurate close to the merger a more quantitative investigation is postponed to future work, where simulations with higher resolution and waveforms corrected for the center of mass drift will be available.

D. EOB-NR comparison: $\phi(\omega)$

Another important means to assess the performance of EOB models is the phase evolution as a function of the frequency. The results of this comparison are shown in Fig. 7. The top panels exhibit the accumulated phase $\phi(\omega)$ with respect to the reference frequency $M\omega_{22} = 0.04$ computed for the EOB_{BBH} model (green), the EOB_{d_yPN} model (orange), and the NR data (black). The difference between the NR and the EOB results is shown in the bottom panels. In contrast to the small tidal contributions in the time evolution of the phase $\phi(t)$, the accumulated phase as a function of frequency due to tidal effects is of the order of 10 to 40rad for our setups, which enables an easier assessment of tidal effects. Furthermore, because no alignment is needed for comparisons of $\phi(\omega)$, the point-mass results EOB_{BBH} can readily be included in the comparison.

The qualitative behavior of $\phi(\omega)$ -plots is the following. Because the frequency increases during the inspiral, the accumulated phase within a given frequency interval $\Delta(M\omega)$ decreases, i.e. $\partial_\omega^2\phi(\omega) < 0$. The effect of the EOSs (seen in Fig. 7 by comparing SLy and MS1b configurations) is that MS1b setups merge at lower frequency due to their smaller compactness. This is in agreement with the conclusions drawn from the results of the binding energy in Sec. IV. Considering the difference $\phi_{\text{NR}} - \phi_{\text{EOB}_{\text{BBH}}}$, shown as the green curves in the lower panels of Fig. 7, we see that smaller total masses lead to a larger accumulated phase due to the larger tidal effects. The oscillatory behavior of $\Delta\phi$ for low frequencies is caused by the residual eccentricity that is not entirely eliminated by the low-pass filter, cf. Appendix B.

In contrast to the results for $\phi(t)$ shown in Fig. 4 the results for $\phi(\omega)$ in Fig. 7 clearly exhibit a substantial improvement of the EOB_{d_yPN} and EOB_{ad_{GSF}+} models over the EOB_{ad_{PN}} model that has a larger discrepancy to the NR results. As described before the agreement between EOB and NR is generally better for softer EOSs for which tidal effects are smaller. But when considering the evolution of $\phi(\omega)$, where differences are more pronounced, it is apparent that several models are outside the NR uncertainty. Only for the cases SLy-153122 and SLy-165110 are the EOB_{d_yPN} results in agreement with the NR waveforms to within the current uncertainty in

NR data. Interestingly, we observe that for some setups the dephasing of the EOB_{ad_{GSF}+} model decreases close to the merger, and, in one case terminates before attaining the merger frequency. These features indicate that the EOB_{ad_{GSF}+} model likely overestimates tidal effects in the late inspiral for these particular cases.

VII. CURRENT PROBLEMS AND FUTURE PROSPECTS

A. Test cases

Having presented the results of comparing EOB predictions to NR results for a variety of systems in the previous sections, we next perform a more detailed analysis to identify the source of the discrepancies. For simplicity, we focus on two complementary cases at opposite corners in the parameter space considered here: SLy-138138, where both stars have a soft EOS and equal masses, and MS1b-165110, where both stars have a stiff EOS and the mass ratio is $q = 1.5$.

1. SLy-138138

In Fig. 8 we summarize important quantities for SLy-138138. In the top panels we show three snapshots of the rest-mass density ρ obtained from the NR simulation, where the color bar is identical to that used in Fig. 1. The snapshots correspond to times $t = 1500M$ (blue), $2500M$ (green) and the moment of merger $2675M$ (red). The other panels show the real part and amplitude of the GW, the dephasing of the EOB models with respect to the NR simulation, the difference of the binding energy between the EOB models and the NR simulation, and the dephasing as a function of the frequency. The retarded time, angular momentum, and frequency corresponding the density snapshots are marked as columns of the same color in the plots.

For setup SLy-138138 both stars have a soft EOS and the same gravitational mass of $M = 1.375$. The tidal coupling constant at $t = 0$ is $\kappa_2^T = 65$. Within our data set this configuration has the smallest tidal effects. Consequently, differences between the EOB models and the NR simulation are also small.

At time $t = 1500M$ (left density snapshot, blue columns) the two stars are well-separated and no tidal deformation is visible. The low density regions ($\rho \lesssim 10^{-8}$, dark shades of blue) in the plot are affected by the artificial atmosphere in the NR treatment and no clear star surface exists. The imprint of the artificial atmosphere decreases for increasing resolution. At this time the tidal EOB models are in agreement with the NR simulation for all quantities considered.

As the system evolves and the separation decreases tidal effects become larger. At $t = 2500M$ (middle density snapshot, green columns) the tidal deformation of

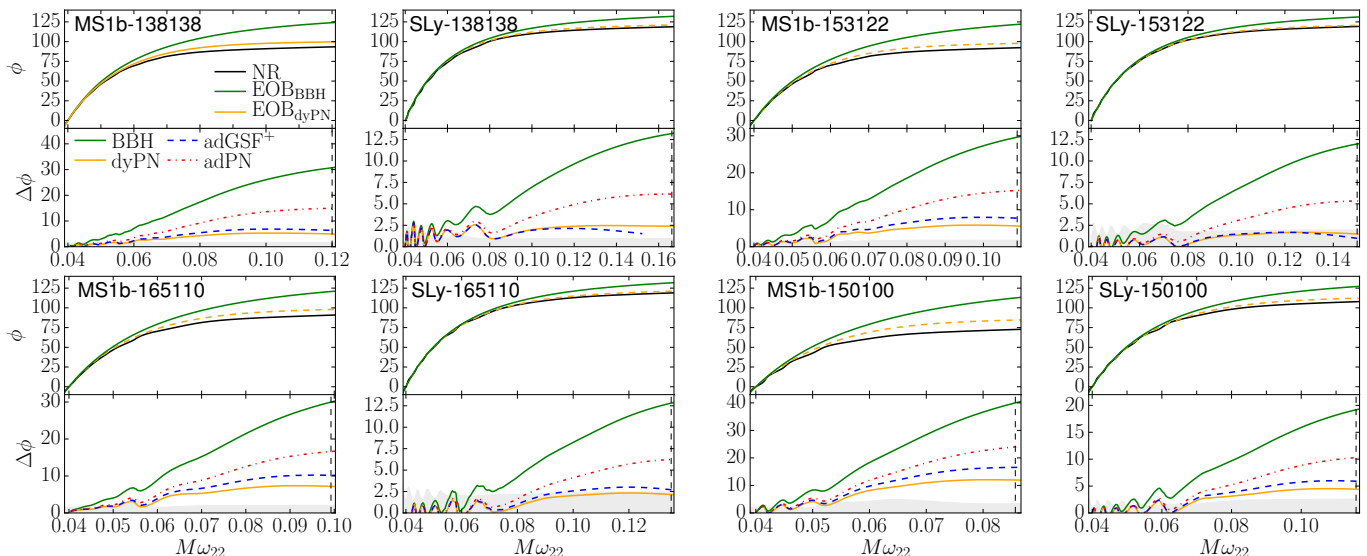


FIG. 7: Phase evolution as a function of GW frequency. The top panels show the evolution of the phase of the (2,2) mode for the NR data (black), the EOB_{BBH} model (green), and the EOB_{dyPN} model (orange) as a function of the dimensionless GW frequency $M\omega_{22}$. The bottom panels show the difference $\Delta\phi = \phi_{\text{EOB}} - \phi_{\text{NR}}$ for all EOB models in rads. The shaded region represents the estimate of the uncertainty of the NR results. The vertical dashed lines in the bottom panels mark the moments of merger for the NR data.

the stars is visible. At this stage the GW phasing predicted by the EOB_{adPN} model starts to deviate from the NR data as seen in the plots of $\Delta\phi(t)$ and $\Delta\phi(\omega)$. This indicates that the EOB_{adPN} model underestimates tidal effects.

Approximately 1.5 orbits later the GW amplitude reaches its maximum and the stars merge (red frame/columns). Because of the enhanced tidal effects in $\text{EOB}_{\text{adGSF}^+}$ and EOB_{dyPN} these models are able to describe the GW phase as a function of time up to the last GW cycle before the merger. We note three important observations: (i) The model $\text{EOB}_{\text{adGSF}^+}$ predicts a merger at a higher specific orbital angular momentum (endpoint of the blue dashed curve in the fourth panel) than the model EOB_{dyPN} . The merger of the NR simulation lies between both models. (ii) The dephasing $\Delta\phi_{\text{EOB}_{\text{adGSF}^+}}(\omega)$ decreases shortly before merger, which is caused by the fact that the binary separation approaches the light ring and tidal effects are overestimated at this stage. (iii) Since tidal effects are overall small, both models $\text{EOB}_{\text{adGSF}^+}$ and EOB_{dyPN} give a reasonably accurate representation of the dynamics and waveform. Further improvements of tidal EOB models in this part of the parameter space would require more accurate NR simulations.

2. MS1b-165110

Figure 9 illustrates the results for the system MS1b-165110 in a similar way as Fig. 8 does for SLy-138138.

At time $t = 1500M$ (left density snapshot) both stars are clearly separated, however, because of the small com-

pactness of the lower-mass star and a stiff EOS, tidal effects are already visible at this early stage of the simulation. Furthermore, the lower density regions are more affected by the artificial atmosphere, showing that the simulation of MS1b-165110 is less accurate than SLy-138138 and leading to larger NR uncertainties. We find that at $t = 1500M$ all EOB models are able to describe the dynamics and GW emission of this system.

Up to a time $t \approx 2300M$ all tidal EOB models remain within the NR error estimate and hence consistent with the simulation. At this time the NSs are still separated. Some of the low density material in the NR simulation is transferred from the secondary to the more massive NS, however, as shown in [56] this mass transfer is in part a numerical artifact that decreases with increasing resolution. Later, at $t = 2500M$ or about two orbits before the merger (middle density snapshot) tidal deformations are significant and the EOB models deviate from the NR models.

Around merger the lower-mass star is tidally disrupted by the primary star (right density snapshot). Tidal effects are significantly larger than for SLy-138138. The dephasing caused by tidal effects ($\Delta\phi_{\text{EOB}_{\text{BBH}}}(\omega)$) is of the order of 30 radians, i.e. more than a factor of two larger than for SLy-138138 (although the system merges at a smaller GW frequency). Overall, during the last four GW cycles before the merger none of the EOB models give a representation that is in agreement with the NR uncertainty. Neither the enhanced tidal effects due to the GSF^+ -potential nor the dynamical tides of EOB_{dyPN} are strong enough for an accurate modeling, although again the EOB_{dyPN} performs better than the $\text{EOB}_{\text{adGSF}^+}$ model. Our results suggest that an additional enhance-

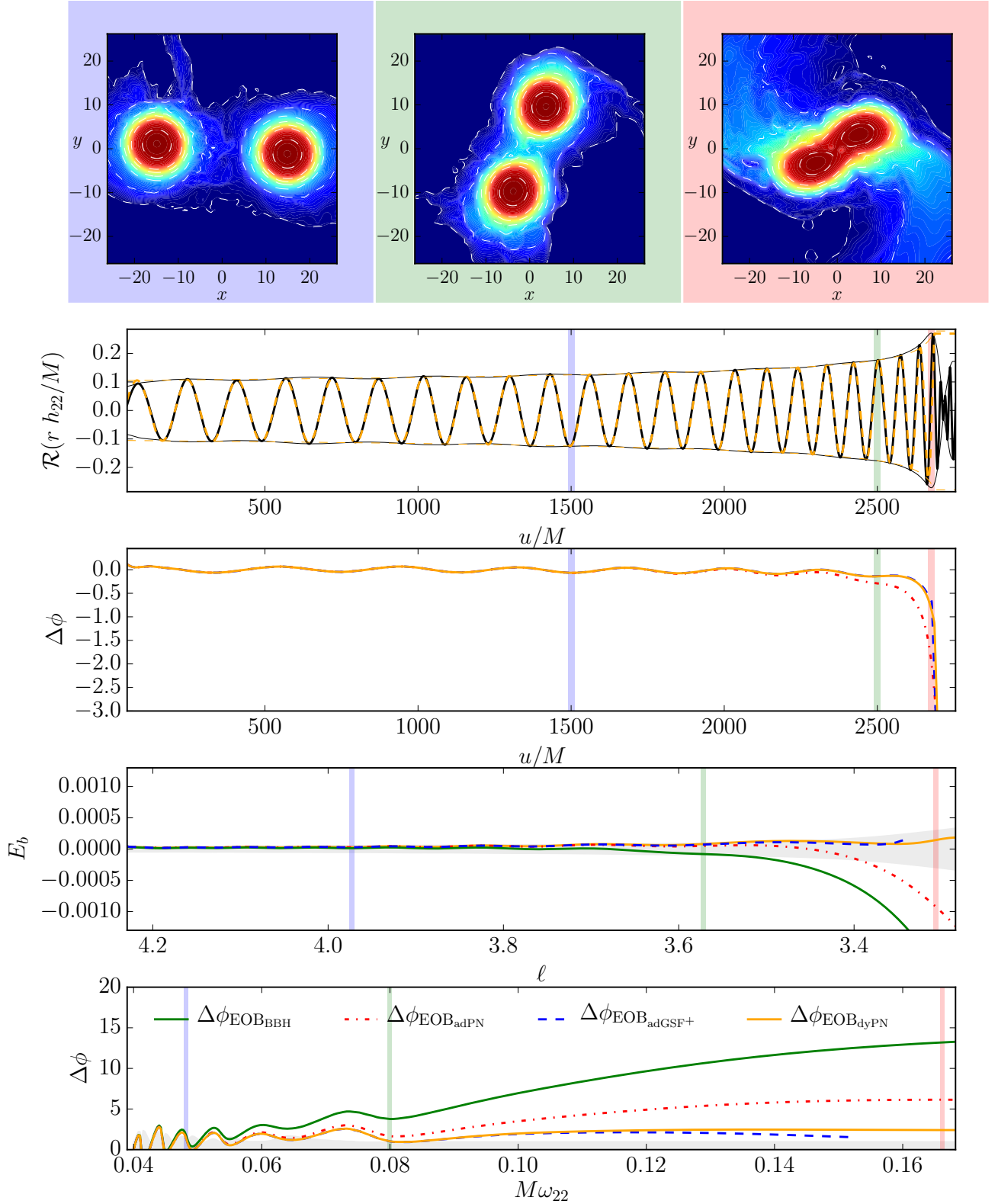


FIG. 8: The top row shows rest-mass density snapshots with the color bar ranging from 10^{-9} (dark blue) to $10^{-2.8}$ (dark red) for SLy-138138. White dashed lines show contour densities lines with $10^{-9}, 10^{-8}, 10^{-7}, 10^{-6}, 10^{-5}, 10^{-4}, 10^{-3}$. The snapshots correspond to times $t = 1500M$ (blue), $2500M$ (green), and the moment of merger $2675M$ (red). The second row shows the real part and the amplitude of the GW for the NR data (black) and EOB_{dyPN} (orange). The third row shows the the dephasing of the EOB models with respect to the NR simulation. The fourth row shows the difference of the binding energy between the EOB models (including green EOB_{BBH}) and the NR simulation. The fifth row shows the dephasing as a function of the frequency. In all panels we use the same color scheme for all models. The times corresponding to the snapshots are marked as shaded regions. The $E(\ell)$ and $\phi(\omega)$ curves end at the moment of merger for all EOB models, which is the reason why for $\text{EOB}_{\text{adGSF+}}$ $E(\ell)$ and $\phi(\omega)$ terminate before the NR merger.

ment of tidal effects in the EOB description for such regions of the BNS parameter space is needed.

B. Towards improved EOB models

The studies presented in this paper [20170207] show that for the region of the BNS parameter space and length of NR simulations considered here both the EOB_{dyPN} and $\text{EOB}_{\text{adGSF+}}$ tidal EOB models provide a robust description of BNSs during most of the inspiral, however, our NR simulations reveal weaknesses of the models in the last few orbits before the merger. In particular, for cases where tidal effects are large i.e. for large κ_2^T , the EOB models tend to underestimate tidal effects irrespective of the mass ratio. To quantify the impact of these differences on measurements with advanced GW detectors requires parameter estimation studies that are the subject of ongoing work, see also [86–88]. Nevertheless, understanding and improving waveform models in the regime close to merger will be essential for future GW detectors. Thus, we want to mention three possibilities for advancing existing models in this part of the BNS parameter space.

1. Combining Dynamical tides with the GSF-inspired potential: $\text{EOB}_{\text{dyGSF+}}$

As discussed above, the current description of tidal effects in the EOB_{dyPN} model tends to underestimate tidal effects in the late inspiral. To illustrate the effect of a simple enhancement of tidal contributions near the merger, we exchange the PN A -Potential with the GSF inspired potential introduced in Sec. II C. This leads to a combination of $\text{EOB}_{\text{adGSF+}}$ and EOB_{dyPN} : $\text{EOB}_{\text{dyGSF+}}$. For this combination, the light ring r_{LR} is computed from Eq. (17) but with the potential $\tilde{A} = A_{\text{pp}} + A_{\text{dyPN}}^{\text{tidal}}$. While $\text{EOB}_{\text{dyGSF+}}$ allows a more accurate representation of systems with large κ_2^T it also enhances tidal effects for systems with small κ_2^T and leads to problems. The effect of using the combination $\text{EOB}_{\text{dyGSF+}}$ is presented in Fig. 10, where the tidal part of the EOB A -potential is shown atop the phasing plots. The configurations are SLy-138138 (left panels) and MS1b-165110 (right panels), i.e. the two cases discussed in detail before.

As seen from the right panels, the $\text{EOB}_{\text{dyGSF+}}$ model has a smaller dephasing from the NR results for systems with large κ_2^T than the other models. In fact it is only for SLy-138138 that the dephasing of $\text{EOB}_{\text{dyGSF+}}$ is comparable to $\text{EOB}_{\text{adGSF+}}$ and EOB_{dyPN} , while for all other setups $\text{EOB}_{\text{dyGSF+}}$ represents the NR data better than the current models (not shown here).

However, overestimating tidal effects for SLy-138138 is a substantial weakness of this ad-hoc combination of dynamical tides and the GSF inspired potential. While several possibilities to overcome these issues exist, a preferable approach that we will pursue in the future is to first

understand and incorporate additional physical effects.

2. Including additional physical effects

As demonstrated by the detailed analyses in this paper [20170207], improvements to tidal EOB models for the late inspiral will require including additional physical effects that are missing from the current descriptions. For example, existing tidal EOB models assume that the NSs are described as separated objects up to the merger. We showed in Fig. 1, Fig. 8, and Fig. 9 that the low density material of the two NSs comes into contact already well before the merger. Subsequently, yet still prior to the merger, the tidally deformed high-density cores of the NSs are moving inside the viscous material from the former NS outer layers. These physical effects must be taken into account in the tidal EOB models. However, a caveat with this conclusion is the fact that with increasing NR resolution and improved numerical methods the NS’s surface becomes less ‘smeared out’ and the interaction of the low density material decreases. Therefore, we postpone a detailed modeling of these near-merger effects to future work, where we will consider NR simulations with even higher resolution than presented here.

3. Calibrating to NR waveforms

Finally, an improvement of the tidal EOB models could also be achieved by incorporating information from NR simulations as done for EOB models for BBH coalescences, see e.g. [37, 39, 89]. Calibrating to NR data entails introducing additional terms into the models and determining their coefficients by maximizing the overlap between the EOB and NR waveforms. This approach will require a large set of highly accurate NR simulations and possibly eccentricity reduced data. After calibration the models *have to* be checked against a variety of waveforms covering a large region in the parameter space. This is a challenging task since the unknown EOS and the larger computational cost for general relativistic hydrodynamic simulations make a full coverage of the BNS parameter space substantially more difficult than for BBHs.

VIII. CONCLUSION

In this article we have presented the largest study to date of the performance of tidal EOB models for BNS systems. We considered setups covering a large portion of the BNS parameter space and analyzed variations in the total mass, the mass ratio, and the EOS. Furthermore, we performed a variety of tests to assess the successes and shortcomings of the models by considering several diagnostic quantities, some of which had not been studied in the context of BNSs before.

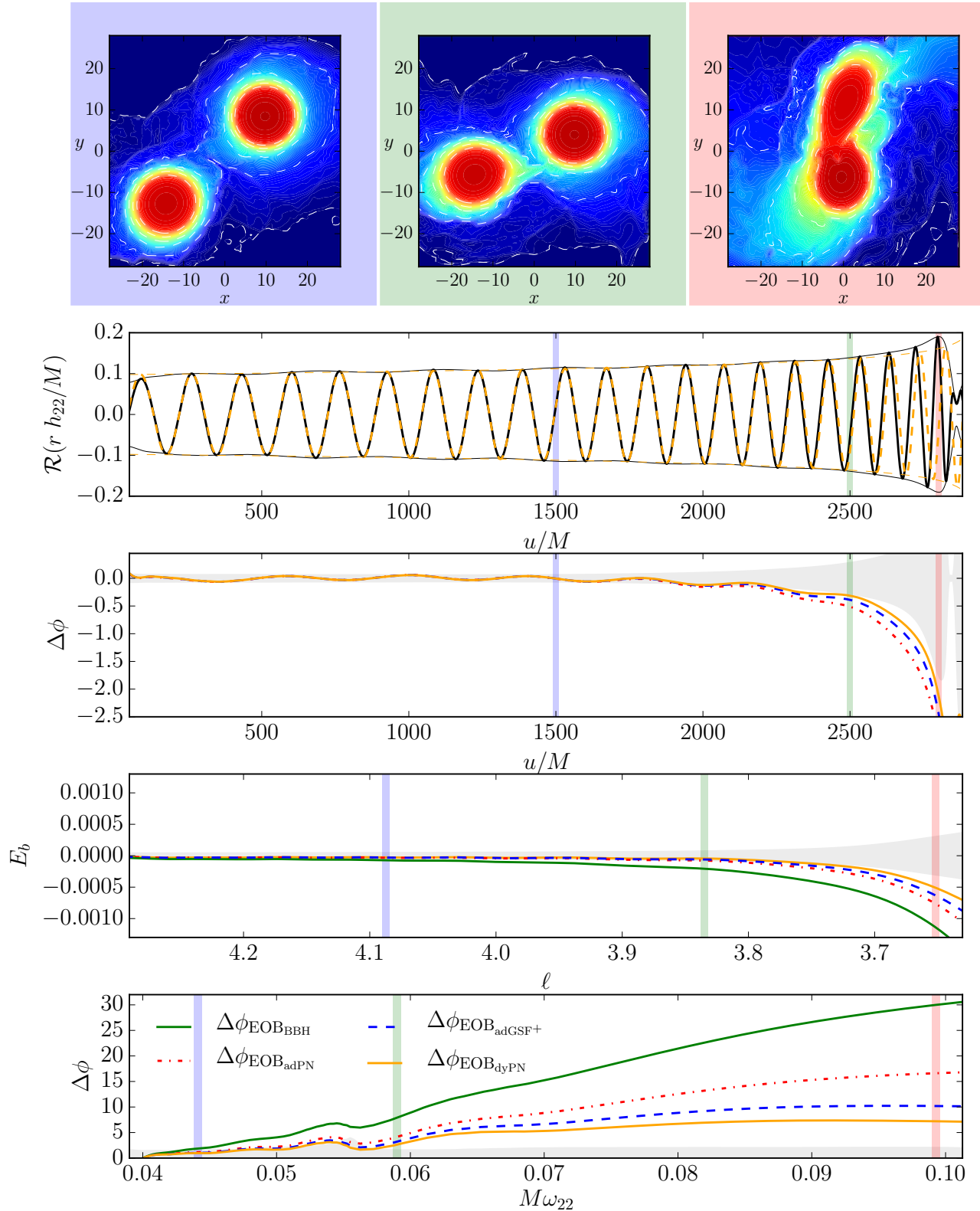


FIG. 9: The top row shows rest-mass density snapshots with the color bar ranging from 10^{-9} (dark blue) to $10^{-2.8}$ (dark red) for MS1b-165110. White dashed lines show contour densities lines with $10^{-9}, 10^{-8}, 10^{-7}, 10^{-6}, 10^{-5}, 10^{-4}, 10^{-3}$. The snapshots correspond to times $t = 1500M$ (blue), $2500M$ (green) and the moment of merger $2802M$ (red). The second row shows the real part and the amplitude of the GW for the NR data (black) and EOB_{dyPN} (orange). The third row shows the the dephasing of the EOB models with respect to the NR simulation. The fourth row shows the the difference of the binding energy between the EOB models (including green EOB_{BBH}) and the NR simulation. The fifth row shows the dephasing as a function of the frequency. In all panels we use the same color scheme for all models. The times corresponding to the snapshots are marked as shaded regions.

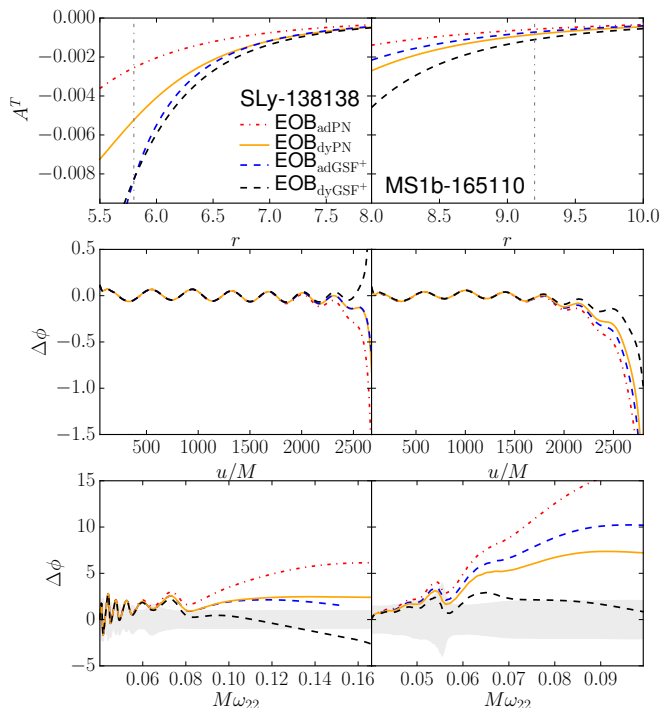


FIG. 10: Top: Tidal contribution to the EOB- A -potential: A^T for SLy-138138 (left) and MS1b-165110 (right). The vertical dashed-dotted line marks the radius r of the EOB_{dyPN} model at the NR merger time. Middle: Dephasing $\Delta\phi(t)$ between the EOB models and NR waveform. Bottom panels: Dephasing $\Delta\phi(\omega)$ between the EOB models and NR waveform.

Our setups encompassed eight different configurations with two different EOSs, three different mass ratios, and two different total masses. We presented comparisons of the energetics of the BNS coalescence characterized by the binding energy vs. specific angular momentum for all models, the periastron advance for one configuration, the time evolution of the GW phase $\phi(t)$ of the (2,2), (2,1), (3,3), and (4,4) modes, and the frequency evolution of the GW phase $\phi(\omega)$ of the (2,2)-mode.

The most effective tool to study the GW signal emitted during the late stage of the BNS coalescence was to compare the accumulated phase within a given frequency interval $\Delta\phi(\omega)$. Considering this quantity enabled studies of the GW phasing without having to align waveforms and emphasized details of the last few orbits before the merger, where tidal effects are strongest.

Overall we found that the EOB_{dyPN} model currently gives the best representation of the dynamics and GWs in the late-inspiral phase, however, the performance of the $\text{EOB}_{\text{adGSF+}}$ model is comparable and differences between the models are small. For all setups the EOB_{adPN} model showed a significantly larger deviation from the NR results. We also found that the mass ratio has only a small influence on the performance of the tidal EOB models. Comparing results for higher modes led to similar results as for the dominant (2,2)-mode. We concluded that the

main limitation of current tidal EOB models is that tidal effects are underestimated for systems with large tidal coupling constants, i.e. those for which tidal effects are largest. This is a characteristic feature of all tidal EOB models which we have tested.

In addition to comparisons between existing tidal EOB models and new state-of-the-art NR simulations, we also outlined possible avenues towards an improved waveform modeling. As a simple extension of the EOB_{dyPN} and the $\text{EOB}_{\text{adGSF+}}$ models we considered the combination of both, i.e. the use of dynamical tides and a GSF inspired potential as a simple way to mimic the larger tidal effects near the merger due to missing physics in the models. Although this method is ‘ad hoc’ and not motivated by the inclusion of additional physical effects, the $\text{EOB}_{\text{dyGSF+}}$ model gives a phase evolution $\phi(t)$ closer to the NR results for almost all cases considered.

We emphasize that besides improving the non-spinning tidal EOB model, an important goal for future work on EOB tidal models is to fully include the effects of spins to achieve a better representation of the inspiral dynamics over a larger region of the BNS parameter space. While first NR simulations have characterized the effect of the NS spin on the GW phasing [77], higher accuracy is needed to place constraints on EOB models, where spin effects for point masses are already incorporated. Further, the extension of the EOB models beyond the moment of merger is of importance and would improve their usability. While first attempts for a post-merger waveform model have been made, e.g. [90], it may also be possible to derive a post-merger model using the same parameters characterizing the inspiral [91].

Finally, we note that determining the priorities for future work on BNS systems will require inputs from data analysis studies. While it is desirable to have an EOB model that exactly reproduces accurate NR results for the GW phasing and energetics up to the merger, it is important to assess the extent to which the discrepancies for some of the setups discussed in this paper would contaminate measurements with LIGO and other ground-based GW detectors. 6

Acknowledgments

It is a pleasure to thank S. Bernuzzi, B. Brügmann, A. Buonanno, B. Lackey, A. Nagar, J. Steinhoff, A. Taracchini, W. Tichy, M. Ujevic for helpful discussion and useful comments on the manuscript. We also want to thank W. Tichy for developing and sharing his SGRID code, S. Bernuzzi and B. Brügmann for allowing us to use the BAM code, A. Taracchini for help with the EOB implementation, and J. Steinhoff for computing the f -mode frequencies. Computations were performed on SuperMUC at the LRZ (Munich) under the project number pr48pu, Jureca (Jülich) under the project number HPO21, Stampede (Texas, XSEDE allocation - TG-PHY140019), and the compute cluster Minerva of

the Max Planck Institute for Gravitational Physics (Albert Einstein Institute).

Appendix A: Eccentricity from NR data

1. Eccentricity from the orbital frequency

The orbital frequency can be approximated from the coordinate location of the two NSs by

$$\Omega(t) = \frac{|\vec{r}(t) \times \dot{\vec{r}}(t)|}{|\vec{r}(t)|^2}, \quad (\text{A1})$$

where $\vec{r}(t)$ is the coordinate distance between the stars' centers. (The center of each star is defined as the minimum of the lapse function inside the star.) Because of the non-zero eccentricity and numerical noise $\Omega(t)$ oscillates during the inspiral. We remove high-frequency noise with a low-pass filter. To extract the eccentricity we fit the orbital frequency according to

$$\Omega_{\text{fit}} = \frac{1}{4}\tau^{-3/8} \left(1 + c_1\tau^{-1/4} + c_2\tau^{-3/8} \right) + (a_1t + b_1)^2 + (a_2t + b_2)^4, \quad (\text{A2})$$

with

$$\tau^2 = \frac{\nu^2(t_c - t)^2}{25M^2} + \tau_0^2, \quad (\text{A3})$$

where a_1 , a_2 , b_1 , b_2 , c_1 , c_2 , t_c , and τ_0 are fitting parameters. Eq. (A2) is based on post-Newtonian calculations, e.g. [92], but extended by $(a_1t + b_1)^2 + (a_2t + b_2)^4$. We find that by adding those terms the final fit is more robust than the choice of [92], i.e. less dependent on the fitting interval and the initial guess of the parameters. In Figure 11 (upper panel) we show the time evolution of $\Omega(t)$ for MS1b-150100. The raw data are presented in black. The eccentricity induced oscillations and smaller high frequency oscillations are clearly visible. We apply a low-pass filter to eliminate the high frequency oscillations (red dashed line) and fit the filtered results with the model function $\Omega_{\text{fit}}(t)$ (blue solid line). The fit depends on the fitting interval and needs to be chosen in a way that the initial junk radiation and gauge dynamics is cut out and that the signal does not extend too close to merger where $\Omega_{\text{fit}}(t)$ loses validity. In Fig. 11 we restricted the fit and the analysis to times $t \in [500M, 3100M]$. The final eccentricity is then given as

$$e_\Omega = \frac{\Omega(t) - \Omega_{\text{fit}}(t)}{2\Omega_{\text{fit}}(t)} \quad (\text{A4})$$

and shown for MS1b-150100 as a blue dash-dotted line in Fig. 11. Due to the emission of GWs the eccentricity decreases over time which can be seen by an increasing amplitude of e_Ω .

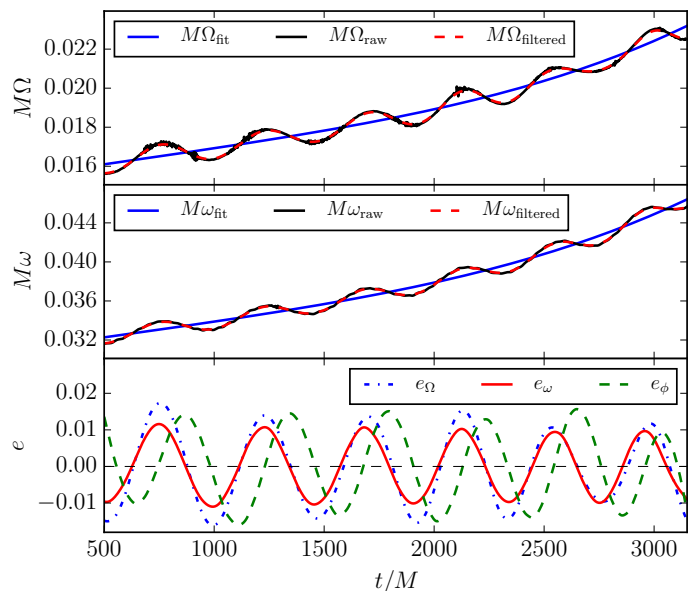


FIG. 11: Eccentricity measures for MS1b-150100. Upper panel: dimensionless orbital frequency $M\Omega$ including the raw NR data (black solid line), low-pass filtered NR data (red dashed line), fitted data according to Eq. (A2) (blue solid line). Middle panel: dimensionless GW frequency $M\omega$ including the raw NR data (black solid line), low-pass filtered NR data (red dashed line), fitted data according to Eq. (A2) (blue solid line). Lower panel: eccentricity measurements from the orbital frequency (blue dash-dotted) GW frequency (red solid) and the GW phase (green dashed).

2. Eccentricity from the GW frequency

In addition to the coordinate location of the two NSs we also use the GW signal to determine the eccentricity. For this purpose we compute the dimensionless GW frequency $M\omega_{22}$. [In the following part of this section, we drop the indices $_{22}$ for the (2,2)-mode for simplicity.] We proceed as for $\Omega(t)$ and apply a low-pass filter. Finally, we fit $M\omega_{\text{filtered}}$ according to Eq. (A2) (blue line), see middle panel of Fig. 11. The eccentricity is then given as

$$e_\omega = \frac{\omega(u) - \omega_{\text{fit}}(u)}{2\omega_{\text{fit}}(u)}. \quad (\text{A5})$$

We present e_ω for MS1b-150100 in the bottom panel of Fig. 11 as a solid red line.

3. Eccentricity from the GW phase

The last eccentricity indicator is based on the phase ϕ of the (2,2)-mode. To extract the eccentricity from the phase evolution, we fit ϕ according to

$$\phi_{\text{fit}} = \sum_{i=0}^6 a_i t^i \quad (\text{A6})$$

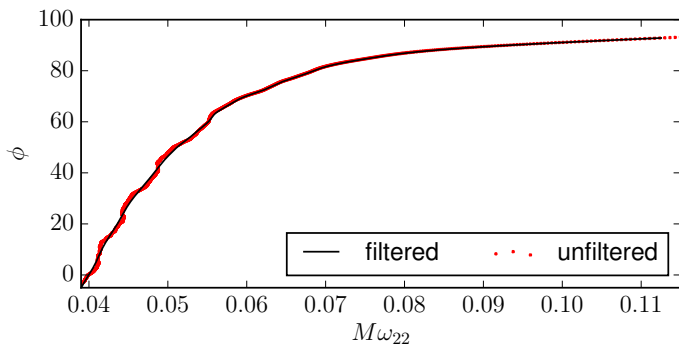


FIG. 12: Computation of $\phi(\omega)$ for MS1b-153122. We present the unfiltered NR data as small red crosses and the interpolated and low pass filtered result as a solid black line. The filtering removes most, but not all, of the eccentricity and numerical noise.

after applying a low-pass filter. The eccentricity is then given as

$$e_\phi = \frac{\phi(u) - \phi_{\text{fit}}(u)}{4}. \quad (\text{A7})$$

The eccentricity e_ϕ for MS1b-150100 is shown in the bottom panel of Fig. 11 as a green dashed line.

Appendix B: Extracting $\phi(\omega)$ from NR data

In previous work we used a non-linear fit of the GW phase to compute the phase evolution as a function of time [77]. This approach is similar to that used for the PA in Appendix A, but more delicate since the fit has to extend up to the merger. To overcome this problem, we use a different method in this work.

The biggest problem is that due to eccentricity and numerical noise $\omega(t)$ might be non-monotonic. We minimize the residual eccentricity with a low-pass filter applied to $\phi(t)$ and $\omega(t)$. Since the eccentricity decreases during the evolution while the phase and frequency evolution accelerates, it is not possible to apply a low pass filter with a fixed cutoff frequency. Therefore we evaluate two different filtered functions and perform a smooth transition between them centered around $M\omega_{22} = 0.055$ (except for MS1b-150100, where we use $M\omega_{22} = 0.053$ since the signal is shorter). As an exemplary case we show the setup MS1b-153122 in Fig. 12, where the raw data are shown as red crosses and the fit as a black line. Notice that the NR data cluster at low frequencies since they are equally spaced in time. Although the filtering reduces the eccentricity, some remaining eccentricity in particular at the transition between the two filtered function can be present. This is the reason for oscillations of $\Delta\phi(\omega)$ in the lower panels of Fig. 7.

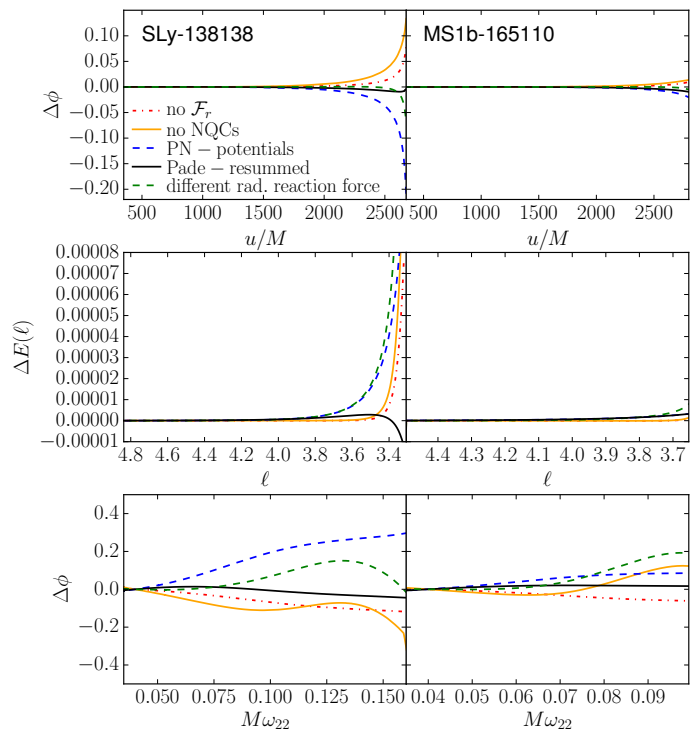


FIG. 13: Influence of the details of the underlying point mass EOB model. As a baseline we use the EOB_{d_{yp}PN} model as employed throughout the paper20170207. We study the effect of NQC correction, the radial radiation reaction force, and the explicit form of the EOB potentials, see text for more details. Top: Dephasing of the (2,2) mode as a function of time in radians for the SLy-138138 setup (left) and the MS1b-165110 setup (right). Middle: Difference in binding energy for $\phi(\omega)$ for SLy-138138 setup (left) and the MS1b-165110 setup (right). Bottom: Dephasing of the (2,2) mode in radians as a function of dimensionless GW frequency for the SLy-138138 setup (left) and the MS1b-165110 setup (right).

Appendix C: Influence of the underlying point mass EOB framework

Although this paper20170207 focuses on the performance of tidal EOB models using different ways of including tidal effects, we also want to briefly quantify the influence of the underlying point mass EOB model during the merger of BNS systems. For this reason we present again results for SLy-138138 and MS1b-165110 as in Sec. VII. The particular effects we study are:

- (i) the radial radiation reaction force \mathcal{F}_r , where we compare results with $\mathcal{F}_r = 0$ as employed in [46, 93] with those that use $\mathcal{F}_r = (p_r/p_\phi)\mathcal{F}_\phi$ as in [47, 61], (shown red in Fig. 13).
- (ii) NQC corrections using the prescription of [61] (shown orange in Fig. 13).
- (iii) calibration and resummation of the potentials, i.e. using simply the PN Taylor expanded EOB potentials (shown blue in Fig. 13).

- (iv) different resummation techniques for the EOB potentials, where we compare a Pade resummation with the calibration summarized in [46] with a logarithmic resummation of the EOB potentials as given explicitly in [48] with the calibration from [37] (shown black in Fig. 13).
- (v) different arguments in the $h_{\ell m}^F$ modes and thus also the radiation reaction force, where we compare results from using, in some occurrences, a different frequency-related variable that was advocated in [94] and is obtained by replacing $\Omega \rightarrow \Omega^3/(\partial H_{\text{EOB}}/\partial p_\phi)^2$ evaluated for circular orbits (shown green in Fig. 13).

Figure 13 summarizes our results. The baseline is the EOB_{d_yPN} model as employed throughout the article. To quantify the effects (i)-(v), we compute the difference in the time evolution of the GW phase (top panels), the binding energy (middle panels), and the phase evolution as a function of the frequency (bottom panels).

Clearly visible is that for all quantities the underlying point mass EOB model effects the SLy-138138 configuration more than the MS1b-165110 setup. This is caused

by the larger compactness and smaller radii of the NSs for SLy-138138, consequently the stars come closer and reach higher frequencies during the inspiral. Considering the differences $\Delta\phi(t) = \phi_{\text{d_yPN}_{\mathcal{F}_r=0}} - \phi_{\text{d_yPN}} > 0$ and $\Delta\phi(t) = \phi_{\text{d_yPN}_{\text{NQC}}} - \phi_{\text{d_yPN}} > 0$ we find that the omission of a radial reaction force or NQC corrections accelerates the inspiral, which mimics larger tidal effects. The opposite is true when using the PN-potentials. The particular resummation technique and argument of the $h_{\ell m}$ modes have only a minor effect on $\phi(t)$.

Considering the binding energy curves, we find that except when using a Pade resummation, all other changes of the underlying point mass EOB model lead to $\Delta E(\ell) > 0$, i.e., the setups are less bound than the EOB_{d_yPN} model used in this work.

Finally, considering the influence of the underlying point mass model on $\phi(\omega)$ we find that all phase differences $\phi(\omega)$ are below 0.5rad. This is significantly smaller than the dephasing accumulated by tidal effects and also significantly smaller than the difference between the EOB_{d_yPN} model and the NR simulations (cf. e.g. bottom panel of Fig. 10).

-
- [1] B. P. Abbott et al. (Virgo, LIGO Scientific), Phys. Rev. Lett. **116**, 061102 (2016), 1602.03837.
 - [2] B. Abbott et al. (Virgo, LIGO Scientific), Phys. Rev. Lett. **116**, 241103 (2016), 1606.04855.
 - [3] J. Aasi et al. (LIGO Scientific Collaboration, Virgo Collaboration), Living Rev. Relativity **19**, 1 (2016), 1304.0670.
 - [4] B. P. Abbott et al. (Virgo, LIGO Scientific) (2016), 1607.07456.
 - [5] J. S. Read, C. Markakis, M. Shibata, K. Uryu, J. D. Creighton, et al., Phys.Rev. **D79**, 124033 (2009), 0901.3258.
 - [6] T. Damour, A. Nagar, and L. Villain, Phys.Rev. **D85**, 123007 (2012), 1203.4352.
 - [7] J. S. Read, L. Baiotti, J. D. E. Creighton, J. L. Friedman, B. Giacomazzo, et al., Phys.Rev. **D88**, 044042 (2013), 1306.4065.
 - [8] W. Del Pozzo, T. G. F. Li, M. Agathos, C. V. D. Broeck, and S. Vitale, Phys. Rev. Lett. **111**, 071101 (2013), 1307.8338.
 - [9] B. D. Lackey and L. Wade, Phys.Rev. **D91**, 043002 (2015), 1410.8866.
 - [10] E. E. Flanagan and T. Hinderer, Phys.Rev. **D77**, 021502 (2008), 0709.1915.
 - [11] T. Hinderer, Astrophys.J. **677**, 1216 (2008), 0711.2420.
 - [12] T. Damour and A. Nagar, Phys. Rev. **D80**, 084035 (2009), 0906.0096.
 - [13] T. Binnington and E. Poisson, Phys. Rev. **D80**, 084018 (2009), 0906.1366.
 - [14] T. Hinderer, B. D. Lackey, R. N. Lang, and J. S. Read, Phys. Rev. **D81**, 123016 (2010), 0911.3535.
 - [15] B. Giacomazzo, L. Rezzolla, and L. Baiotti, Phys. Rev. **D83**, 044014 (2011), 1009.2468.
 - [16] Y. Sekiguchi, Class.Quant.Grav. **27**, 114107 (2010), 1009.3358.
 - [17] Y. Sekiguchi, K. Kiuchi, K. Kyutoku, and M. Shibata, Phys.Rev.Lett. **107**, 051102 (2011), 1105.2125.
 - [18] F. Galeazzi, W. Kastaun, L. Rezzolla, and J. A. Font, Phys.Rev. **D88**, 064009 (2013), 1306.4953.
 - [19] K. Kiuchi, K. Kyutoku, Y. Sekiguchi, M. Shibata, and T. Wada, Phys.Rev. **D90**, 041502 (2014), 1407.2660.
 - [20] K. Dionysopoulou, D. Alic, and L. Rezzolla, Phys. Rev. **D92**, 084064 (2015), 1502.02021.
 - [21] C. Palenzuela, S. L. Liebling, D. Neilsen, L. Lehner, O. L. Caballero, E. O'Connor, and M. Anderson, Phys. Rev. **D92**, 044045 (2015), 1505.01607.
 - [22] L. Lehner, S. L. Liebling, C. Palenzuela, O. L. Caballero, E. O'Connor, M. Anderson, and D. Neilsen (2016), 1603.00501.
 - [23] Y. Sekiguchi, K. Kiuchi, K. Kyutoku, and M. Shibata, Phys.Rev. **D91**, 064059 (2015), 1502.06660.
 - [24] F. Foucart, R. Haas, M. D. Duez, E. OConnor, C. D. Ott, L. Roberts, L. E. Kidder, J. Lippuner, H. P. Pfeiffer, and M. A. Scheel, Phys. Rev. **D93**, 044019 (2016), 1510.06398.
 - [25] Y. Sekiguchi, K. Kiuchi, K. Kyutoku, M. Shibata, and K. Taniguchi, Phys. Rev. **D93**, 124046 (2016), 1603.01918.
 - [26] S. Bernuzzi, M. Thierfelder, and B. Brügmann, Phys.Rev. **D85**, 104030 (2012), 1109.3611.
 - [27] D. Radice, L. Rezzolla, and F. Galeazzi, Mon.Not.Roy.Astron.Soc. **437**, L46 (2014), 1306.6052.
 - [28] D. Radice, L. Rezzolla, and F. Galeazzi, Class.Quant.Grav. **31**, 075012 (2014), 1312.5004.
 - [29] K. Hotokezaka, K. Kyutoku, and M. Shibata, Phys.Rev. **D87**, 044001 (2013), 1301.3555.
 - [30] D. Radice, L. Rezzolla, and F. Galeazzi (2015), 1502.00551.

- [31] K. Hotokezaka, K. Kyutoku, H. Okawa, and M. Shibata, Phys. Rev. **D91**, 064060 (2015), 1502.03457.
- [32] S. Bernuzzi and T. Dietrich, Phys. Rev. **D94**, 064062 (2016), 1604.07999.
- [33] M. Favata, Phys.Rev.Lett. **112**, 101101 (2014), 1310.8288.
- [34] K. Yagi and N. Yunes, Phys.Rev. **D89**, 021303 (2014), 1310.8358.
- [35] A. Buonanno and T. Damour, Phys. Rev. **D59**, 084006 (1999), gr-qc/9811091.
- [36] A. Buonanno and T. Damour, Phys. Rev. **D62**, 064015 (2000), gr-qc/0001013.
- [37] A. Taracchini, A. Buonanno, Y. Pan, T. Hinderer, M. Boyle, et al., Phys.Rev. **D89**, 061502 (2014), 1311.2544.
- [38] Y. Pan, A. Buonanno, A. Taracchini, L. E. Kidder, A. H. Mroue, et al., Phys.Rev. **D89**, 084006 (2014), 1307.6232.
- [39] T. Damour and A. Nagar, Phys.Rev. **D90**, 044018 (2014), 1406.6913.
- [40] T. Damour and A. Nagar, Phys. Rev. **D81**, 084016 (2010), 0911.5041.
- [41] J. E. Vines and E. E. Flanagan, Phys. Rev. **D88**, 024046 (2010), 1009.4919.
- [42] L. Baiotti, T. Damour, B. Giacomazzo, A. Nagar, and L. Rezzolla, Phys. Rev. Lett. **105**, 261101 (2010), 1009.0521.
- [43] D. Bini, T. Damour, and G. Faye, Phys.Rev. **D85**, 124034 (2012), 1202.3565.
- [44] S. Bernuzzi, A. Nagar, M. Thierfelder, and B. Brügmann, Phys.Rev. **D86**, 044030 (2012), 1205.3403.
- [45] D. Bini and T. Damour, Phys.Rev. **D90**, 124037 (2014), 1409.6933.
- [46] S. Bernuzzi, A. Nagar, T. Dietrich, and T. Damour, Phys.Rev.Lett. **114**, 161103 (2015), 1412.4553.
- [47] T. Hinderer et al., Phys. Rev. Lett. **116**, 181101 (2016), 1602.00599.
- [48] J. Steinhoff, T. Hinderer, A. Buonanno, and A. Taracchini, Phys. Rev. **D94**, 104028 (2016), 1608.01907.
- [49] J. K. Swiggum et al., Astrophys. J. **805**, 156 (2015), 1503.06276.
- [50] J. M. Lattimer, Ann. Rev. Nucl. Part. Sci. **62**, 485 (2012), 1305.3510.
- [51] J. G. Martinez, K. Stovall, P. C. C. Freire, J. S. Deneva, F. A. Jenet, M. A. McLaughlin, M. Bagchi, S. D. Bates, and A. Ridolfi, Astrophys. J. **812**, 143 (2015), 1509.08805.
- [52] P. Lazarus et al. (2016), 1608.08211.
- [53] M. Dominik, K. Belczynski, C. Fryer, D. E. Holz, E. Berti, T. Bulik, I. Mandel, and R. O’Shaughnessy, Astrophys. J. **759**, 52 (2012), 1202.4901.
- [54] T. Dietrich, N. Moldenhauer, N. K. Johnson-McDaniel, S. Bernuzzi, C. M. Markakis, B. Brügmann, and W. Tichy, Phys. Rev. D **91**, 124007 (2015), 1507.07100.
- [55] D. Hilditch, S. Bernuzzi, M. Thierfelder, Z. Cao, W. Tichy, et al., Phys. Rev. **D88**, 084057 (2013), 1212.2901.
- [56] T. Dietrich, M. Ujevic, W. Tichy, S. Bernuzzi, and B. Bruegmann (2016), 1607.06636.
- [57] EOB-IHES, URL <https://eob.ihes.fr/>.
- [58] E. Barausse, A. Buonanno, and A. Le Tiec, Phys.Rev. **D85**, 064010 (2012), 1111.5610.
- [59] D. Bini and T. Damour, Phys.Rev. **D89**, 064063 (2014), 1312.2503.
- [60] D. Bini and T. Damour, Phys.Rev. **D87**, 121501 (2013), 1305.4884.
- [61] A. Taracchini, Y. Pan, A. Buonanno, E. Barausse, M. Boyle, et al., Phys.Rev. **D86**, 024011 (2012), 1202.0790.
- [62] Taracchini, Andrea and others, *in prep.*, in prep. (2017), in prep.
- [63] S. R. Dolan, P. Nolan, A. C. Ottewill, N. Warburton, and B. Wardell (2014), 1406.4890.
- [64] B. D. Lackey, S. Bernuzzi, C. R. Galley, J. Meidam, and C. Van Den Broeck (2016), 1610.04742.
- [65] W. Tichy, Class.Quant.Grav. **26**, 175018 (2009), 0908.0620.
- [66] W. Tichy, Phys. Rev. D **86**, 064024 (2012), 1209.5336.
- [67] B. Brügmann, J. A. Gonzalez, M. Hannam, S. Husa, U. Sperhake, et al., Phys.Rev. **D77**, 024027 (2008), gr-qc/0610128.
- [68] M. Thierfelder, S. Bernuzzi, and B. Brügmann, Phys.Rev. **D84**, 044012 (2011), 1104.4751.
- [69] T. Dietrich, S. Bernuzzi, M. Ujevic, and B. Brügmann, Phys. Rev. **D91**, 124041 (2015), 1504.01266.
- [70] J. S. Read, B. D. Lackey, B. J. Owen, and J. L. Friedman, Phys. Rev. **D79**, 124032 (2009), 0812.2163.
- [71] F. Douchin and P. Haensel, Astron. Astrophys. **380**, 151 (2001), astro-ph/0111092.
- [72] H. Müller and B. D. Serot, Nucl. Phys. **A606**, 508 (1996), nucl-th/9603037.
- [73] A. Bauswein, H.-T. Janka, and R. Oechslin, Phys.Rev. **D82**, 084043 (2010), 1006.3315.
- [74] N. Moldenhauer, C. M. Markakis, N. K. Johnson-McDaniel, W. Tichy, and B. Brügmann, Phys. Rev. **D90**, 084043 (2014), 1408.4136.
- [75] T. Damour, A. Nagar, D. Pollney, and C. Reisswig, Phys.Rev.Lett. **108**, 131101 (2012), 1110.2938.
- [76] S. Bernuzzi, T. Dietrich, W. Tichy, and B. Brügmann, Phys.Rev. **D89**, 104021 (2014), 1311.4443.
- [77] T. Dietrich, S. Bernuzzi, M. Ujevic, and W. Tichy (2016), 1611.07367.
- [78] S. Bernuzzi, A. Nagar, S. Balmelli, T. Dietrich, and M. Ujevic, Phys.Rev.Lett. **112**, 201101 (2014), 1402.6244.
- [79] S. Bernuzzi, A. Nagar, S. Balmelli, T. Dietrich, and M. Ujevic, J.Phys.Conf.Ser. **610**, 012047 (2015).
- [80] K. Takami, L. Rezzolla, and L. Baiotti, Phys.Rev. **D91**, 064001 (2015), 1412.3240.
- [81] A. Le Tiec, A. H. Mroue, L. Barack, A. Buonanno, H. P. Pfeiffer, N. Sago, and A. Taracchini, Phys. Rev. Lett. **107**, 141101 (2011), 1106.3278.
- [82] T. Hinderer et al., Phys. Rev. **D88**, 084005 (2013), 1309.0544.
- [83] A. H. Mroue, H. P. Pfeiffer, L. E. Kidder, and S. A. Teukolsky, Phys. Rev. **D82**, 124016 (2010), 1004.4697.
- [84] E. T. Newman and P. R., J. Math. Phys. **3**, 566 (1962), , erratum in J. Math. Phys. **4**, 998 (1963).
- [85] C. Reisswig and D. Pollney, Class.Quant.Grav. **28**, 195015 (2011), 1006.1632.
- [86] B. D. Lackey, K. Kyutoku, M. Shibata, P. R. Brady, and J. L. Friedman, Phys.Rev. **D89**, 043009 (2014), 1303.6298.
- [87] L. Wade, J. D. E. Creighton, E. Ochsner, B. D. Lackey, B. F. Farr, et al. (2014), 1402.5156.
- [88] K. Hotokezaka, K. Kyutoku, Y.-i. Sekiguchi, and M. Shibata, Phys. Rev. **D93**, 064082 (2016), 1603.01286.
- [89] A. Boh et al. (2016), 1611.03703.
- [90] J. A. Clark, A. Bauswein, N. Stergioulas, and

- D. Shoemaker, *Class. Quant. Grav.* **33**, 085003 (2016), 1509.08522.
- [91] S. Bernuzzi, T. Dietrich, and A. Nagar, *Phys. Rev. Lett.* **115**, 091101 (2015), 1504.01764.
- [92] M. Hannam, S. Husa, F. Ohme, D. Müller, and B. Brügmann, *Phys. Rev.* **D82**, 124008 (2010), 1007.4789.
- [93] T. Damour, A. Nagar, and S. Bernuzzi, *Phys.Rev.* **D87**, 084035 (2013), 1212.4357.
- [94] T. Damour, B. R. Iyer, and A. Nagar, *Phys. Rev.* **D79**, 064004 (2009), 0811.2069.